

Infrared Spectroscopy of Star Formation in Galactic and Extragalactic Regions

Grant NAG5-10659

Annual Performance Report No. 3

For the period 1 March 2003 through 29 February 2004

Principal Investigator:

Dr. Howard A. Smith

March 2004

Prepared for
National Aeronautics and Space Administration
Washington D.C.

Smithsonian Institution
Astrophysical Observatory
Cambridge, Massachusetts 02138-1596

The Smithsonian Astrophysical Observatory
is a member of the
Harvard-Smithsonian Center for Astrophysics

The NASA Technical Officer for this grant is Dr. Jay Frogel, NASA Headquarters, 300 E Street SW,
Code SR, Washington DC 20546-0001

Table of Contents

I. Program Objectives.....	1
II. Progress Report	1
A. ISO Data Analysis and Modeling.....	1
B. Other Science Results.....	2
C. Advising Students and Postdocs.....	2
D. E&PO Activities.....	2
III. Program Plans.....	2
IV. Reportable Patents/New Technology	2
Appendix A: Publications List.....	A
Appendix B: SIRTf Observations	B
Appendix C: Papers.....	C

I. Program Objectives

In this program we proposed to perform a series of spectroscopic studies, including data analysis and modeling, of star formation regions using an ensemble of archival space-based data from the Infrared Space Observatory's Long Wavelength Spectrometer and Short Wavelength Spectrometer, and to take advantage of other spectroscopic databases including the first results from SIRTf. Our emphasis has been on star formation in external, bright IR galaxies, but other areas of research have included young, low or high mass pre-main sequence stars in star formation regions, and the galactic center. The OH lines in the far infrared were proposed as one key focus of this inquiry because the Principal Investigator (H. Smith) had a full set of OH IR lines from ISO observations. It was planned that during the proposed 2-1/2 year timeframe of the proposal other data (including perhaps from SIRTf) would become available, and we intended to be responsive to these and other such spectroscopic data sets.

The program has the following goals:

- 1) Refine the data analysis of ISO observations to obtain deeper and better SNR results on selected sources. The ISO data itself underwent pipeline 10 reductions in early 2001, and the more "hands-on data reduction packages" have been released. The ISO Fabry-Perot database is particularly sensitive to noise and can have slight calibration errors; improvements are anticipated. We plan to build on these deep analysis tools and contribute to their development.
- 2) Model the atomic and molecular line shapes, in particular the OH lines, using revised montecarlo techniques developed by the Submillimeter Wave Astronomy Satellite (SWAS) team at the Center for Astrophysics.
- 3) Use newly acquired space-based SIRTf or SOFIA spectroscopic data as they become available, and contribute to these observing programs as appropriate.
- 4) Attend scientific meetings and workshops.
- 5) Conduct E&PO activities, especially as related to infrared astrophysics and/or spectroscopy.

The program since its inception has been extremely successful: We presented or submitted more than about a dozen articles, sponsored a workshop, and participated in scientific conferences. The molecular line montecarlo code has undergone important revisions for infrared lines and has made significant predictions. First Spitzer data are available and we have made useful contributions to pending SIRTf science observations. E&PO programs have been active, including the exhibit at Boston's Museum of Science. We anticipate progress to continue in all areas. Detailed descriptions of all these results follow below.

II. Progress Report

We made excellent progress during the past year; however we note that funding for the year's activities did not arrive until last week -- nearly 11 months late. As a result the progress was considerably below our hopes. In the next year we plan to complete the tasks unfinished due to this funding delay.

A. ISO Data Analysis and Modeling

Last year we submitted a paper entitled "The Far Infrared Lines of OH as Molecular Cloud Diagnostics" to the 2nd Maryland Conference on Far IR Astronomy, 2002, and also presented an improved version of "The Infrared Lines of OH: Diagnostics of Molecular Cloud Compositions in Infrared Bright Galaxies," to the *Proceedings of the Workshop of the Neutral ISM in Starburst Galaxies*, Marstrand, Sweden, 2003. This analysis was based on the SWAS montecarlo code modeling of the OH lines in galaxies observed by ISO (Figure 1). Since that meeting last spring considerable effort has been put into improving the montecarlo code. A group of European astronomers, including Dr. Pepe Chernicharo and Prof. Eduardo González-Alfonso, had been performing montecarlo modeling of other molecules seen in ISO galaxies. We used portions of this grant to bring Prof. González to Cambridge

for an intensive working visit. The result of that work is the paper in Appendix C on Arp220, now submitted to ApJ.

In a second major paper on the IR spectroscopy of galaxies, we are about to submit a paper on the spectroscopy on NGC 1068, the archetypal Seyfert 2 galaxy (Figure 2). One of the dramatic results in our work is the discovery that **ALL** of the OH lines seen there are seen in emission, making this source unique. A preprint is attached in Appendix C.

B. Other Science Results

SIRTF: SIRTF science development was the other major component of this year's research. This program supported the development of five "Early Release Objects" for SIRTF observations on which Dr. Smith was Principal Investigator or Co-Investigator, and another 5 proposals for GO time. The early release program is designed to rapidly present to the public and the scientific community some exciting results from Spitzer in the first months of its operation. The Spitzer instrument and science teams submitted proposals for ERO objects, and a competitive selection process narrowed these down to a small group with exciting science and realistic observational parameters. This grant supported Dr. Smith's participation in the ERO process, including developing science goals, identifying key objects for observation, and developing the detailed AOR (observing formulae) to be used by the instruments for mapping, integrating, etc.

Appendix B lists the Spitzer programs involved.

C. Advising Students and Postdocs

During this year we had one graduate student, Idan Ginsburg, who participated in the modeling of the continuum of galaxies using the montecarlo code and who wrote a C++ script to facilitate this work. We also supervised the visit of Dr. Eduardo González-Alfonso, who likewise worked on the galaxy modeling (reprints attached).

D. E&PO Activities

During this period the PI gave several talks to elementary school groups, as well as to a summer camp.

III. Program Plans

During the final year of this program, much of which has been delayed because funding arrived eleven months late, we intend to bring to closure the projects discussed to date:

- 1) Reduction of the ISO galaxy data set using the Chernicharo/González algorithms;
- 2) Modeling the OH lines with the corrected and improved montecarlo code;
- 3) Tightening the arguments made in our earlier article -- that there are three types of active/IRB galaxies as typified by the kinds of molecular clouds that dominate their FIR emission: large diffuse clouds as in normal IRBs; smaller, more dense clouds as in Arp 220 and other mixed AGN; and very dense small cloudlets as seen in the Seyfert galaxy NGC 1068;
- 4) Spitzer activities: We will continue to be active in E&PO and GO, including an aggressive IRAC/Spitzer E&PO effort.

IV. Reportable Patents/New Technology

There have been no reportable patents/new technology made under this grant.

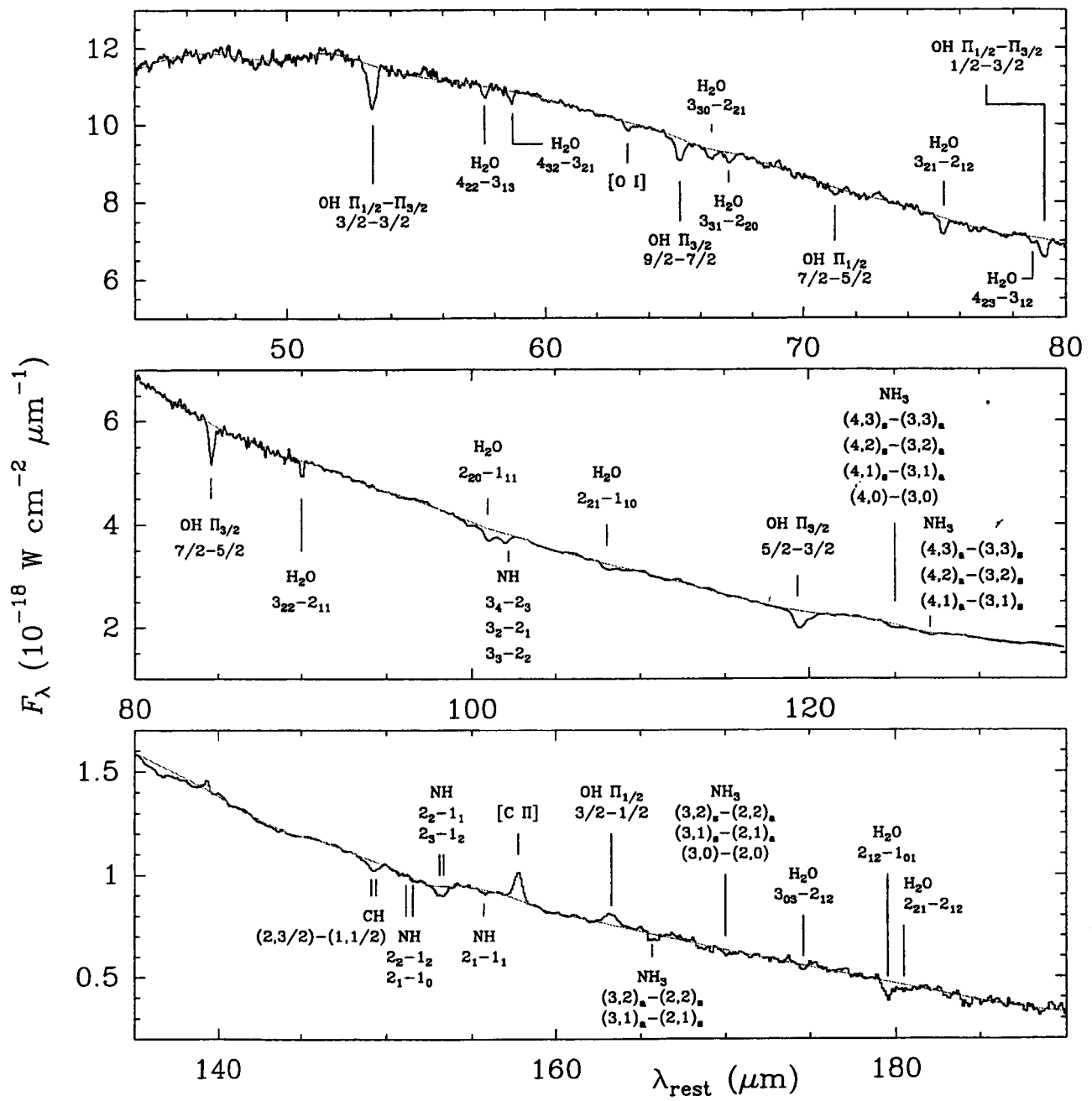


Fig. 1.— ISO/LWS spectrum of Arp 220, where the most prominent line features are identified (see text). The grey line shows the adopted baseline (continuum level).

Figure 1

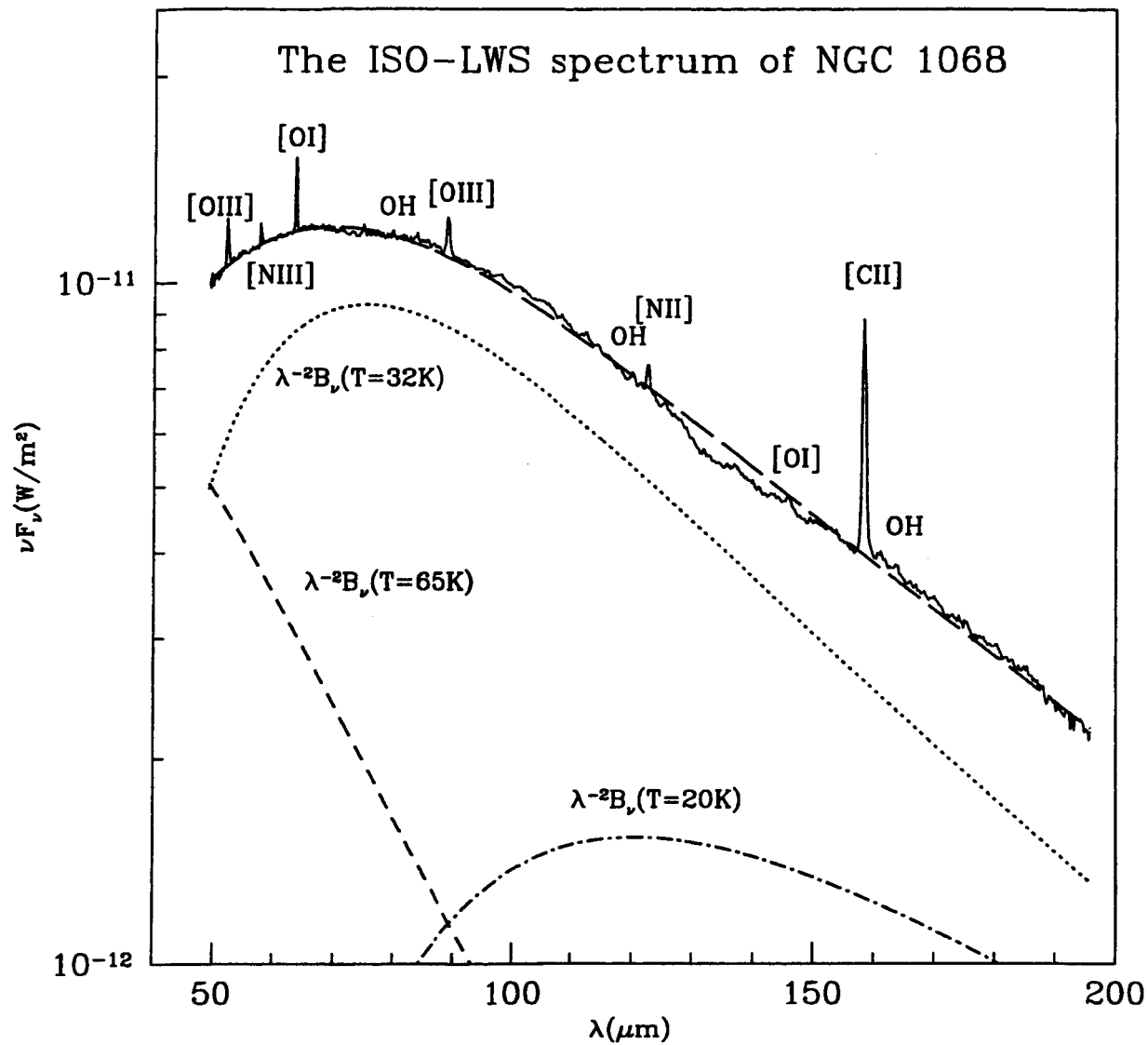


Fig. 1.— The ISO-LWS spectrum of NGC1068. The long-dashed line, which is fitting the data (reduced $\chi^2=0.40$, corresponding to a probability of $P>98\%$) represents the sum of the three different grey-body functions: dotted line: main component at $T=32\text{K}$; dotted-dashed line: cold component at $T=20\text{K}$; short-dashed line: warm component at $T=65\text{K}$.

Appendix A: Publications List

- "Mid and Far Infrared Spectroscopy of Seyfert Galaxies," Spinoglio, L., Malkan, M., Smith, H.A., Fischer, J., in the ASP Conference Series, *Active Galactic Nuclei: from Central Engine to Host* (Meudon, France) July 23-27, 2002, eds: Colin, Combes and Shlosman, Vol. 290, p. 557, 2003
- "Designer Infrared Filters Using Stacked Metal Lattices," Smith, H.A., Rebbert, M., and Sternberg, O., *App. Phys. Lett.*, **82**, 3605, 2003
- "Public Attitudes Towards Space Science," Smith, H.A., *Space Science Reviews*, **105**, 1-2,493, 2003
- "The Far-Infrared Emission Line and Continuum Spectrum of the Seyfert Galaxy NGC 1068," Spinoglio, L., Malkan, M., Smith, H.A., Fischer, J., submitted to *ApJ* (2003)
- "Infrared Filters Fabricated from Metal Grids Allow Easy Tailoring of the Filters' Optical Properties," Smith, H.A., *Laser Focus World*, June 2003
- "Transmittance of Thick Metal Meshes of Various Shapes and Thicknesses in the Infrared Wavelength Region," Sternberg, O., Shah, J., Moller, J., Grebel, H., Stewart, K., Fischer, J., Rebbert, M., Smith, H.A., and Fettig, R., *TDW2003: International Workshop on Thermal Detectors for Space Based on Planetary, Solar and Earth Science Applications*, 2003
- "The Infrared Lines of OH: Diagnostics of Molecular Cloud Compositions in Infrared Bright Galaxies," Smith, H.A., González-Alfonso, E., Fischer, J., Ashby, M., Dudley, C., and Spinoglio, L., in *Proceedings of the Workshop of the Neutral ISM in Starburst Galaxies*, Marstrand, Sweden, 2003
- "The Effects of Dust in Infrared Luminous Galaxies: An Integrated Modeling Approach," Satyapal, S., Dudley, C., Fischer, J., Luhman, M., Smith, H. A., *Astrophysics of Dust*, Estes Park, Colorado, May 26 - 30, Edited by Adolf N. Witt, 2003
- "Designer Infrared Filters Using Stacked Metal Lattices," Smith, H. A., Sternberg, Stewart, Fischer, Rebbert, Henry, Moller, *Frontiers of High Resolution Spectroscopy*, 25th meeting of the IAU, Joint Discussion 20, Sydney, Australia, 2003
- "The Far Infrared Lines of OH as Molecular Cloud Diagnostics," Smith, H. A., Ashby, Fischer, González, Spinoglio, Dudley, *The Astrochemistry of External Galaxies*, 25th meeting of the IAU, Joint Discussion, Sydney, Australia, 2003
- "The Far Infrared Spectrum of Arp 220," González-Alfonso, E., Smith, H., Fischer, J., and Cericharo, J., submitted to *ApJ*
- "First Extragalactic Science from IRAC, The Infrared Array Camera on SST," Willner, S., ... Smith, H., *et al.*, BAAS, 2004
- "First Galactic Images from IRAC, SST's Infrared Array Camera," Megeath, T., ... Smith, H., *et al.*, BAAS, 2004

Appendix B: *SIRTF* Observations

Spitzer ERO Programs

- 1) IRAC Images of an Infrared Bright Galaxy: M82
- 2) IRAC/IRS Early Release Observations of RCW 108
- 3) Observations of Interacting Galaxies
- 4) *SIRTF* Observations of the Galactic Center
- 5) Extremely Red Background Objects in the IRAC Survey

Spitzer GO Proposals

- 6) The Spitzer Interacting Galaxy Sample
- 7) The Low Redshift 3CRR Sources
- 8) Probing the Dynamical Causes of the Morphological Butcher-Oemler Effect
- 9) IRS Spectroscopy of a Complete Sample of Active and Starburst Galaxies
- 10) Neon, Sulfur and Discrepant Abundance Gradients in M33
- 11) Measuring the Veil: Galactic Extinction

Appendix C: *Papers*

- 1) **The Infrared Lines of OH: Diagnostics of Molecular Cloud Conditions in Infrared Bright Galaxies.**
- 2) **The Far-Infrared Spectrum of Arp 220**
- 3) **The Far-Infrared Emission Line and Continuum Spectrum of the Seyfert Galaxy NGC 1068**

****TITLE****

*ASP Conference Series, Vol. **VOLUME**, **PUBLICATION YEAR***

****EDITORS****

The Infrared Lines of OH: Diagnostics of Molecular Cloud Conditions in Infrared Bright Galaxies

Howard A. Smith(1), Eduardo Gonzalez-Alfonso(1,2), Jackie Fischer(3), Matthew L.N. Ashby (1), Chris Dudley(3), and Luigi Spinoglio(4)

(1)Harvard-Smithsonian Center for Astrophysics, 60 Garden Street, Cambridge, MA 02138, (2)Universidad de Alcala, Spain. (3)Naval Research Laboratory, Washington, DC 20375, (4)Istituto di Fisica dello Spazio Interplanetario, CNR, Italy

Abstract. ISO detected 9 of the 15 far-IR lines of OH that arise between the molecule's lowest 8 rotational levels. The lines were seen, sometimes in emission and sometimes in absorption, in a wide variety of galactic and extragalactic objects ranging from AGB stars to molecular clouds in AGN and LIRGs. This set of OH lines provides an important diagnostic for many reasons: they span a wide wavelength range (from 28.9 μ m to 163.2 μ m); the transitions have fast radiative rates; the abundance of OH is relatively high; the IR continuum plays an important role as a pump; the contribution from shocks is relatively minor; and, not least, the strong cm-wave radiation from OH allows comparison with VLBI datasets. OH plays a key role in the chemistry of the ISM. We have used montecarlo and non-local radiative transfer codes to analyze the spectra of a number of LIRGs with excellent success. Other detected lines in the ISO spectra, including those from H_2O , CH, NH_3 , CO, [CII] and [OI], are also modeled by the codes, as is the continuum.

1. Characteristics of clouds in LIRGs as inferred from their OH lines

ISO-LWS detected OH in emission and/or absorption in: Arp 220, Cen A, IRAS17208-0014, IRAS20100-4156, M82, Mkn 231, Mkn 273, NGC 253, NGC 891, NGC 1068, NGC 1614, NGC 3690A, NGC 4945, NGC 7469, and 3Zw35. Perhaps the most striking result from the observed set of extragalactic lines is their wide range of behavior, even though all arise in LIRGs with either active star formation, an active nucleus, or perhaps both. In Arp 220, for example, every OH line is seen in absorption except the longest wavelength, 163 μ m line which is seen weakly in emission (Gonzalez-Alfonso et al., 2004; Fischer et al., "Proc.ISO to the Peaks Workshop," 1998). By contrast, in NGC 1068 every detected line is seen in emission, even the strong 119 μ m transition between ground and the first excited state (Spinoglio et al., 2004). NGC 253, a nearby starburst, has some OH lines in emission and some in absorption (Bradford et al., "Proc.The Universe as Seen by ISO," 1999; Smith et al., "Proc. 2nd Md. Conference on FIR Astronomy," 2004), while in M82, the infrared bright, prototype starburst galaxy, the lines' equivalent widths are so small that even with

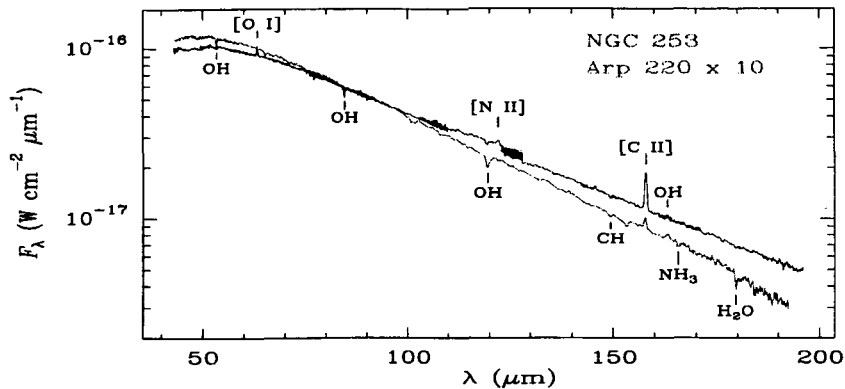


Figure 1. The full ISO-LWS spectra of NGC 253 (strong [CII]) and Arp220 (strong water), with the prominent features marked. The continua and all the features are well modeled (from Gonzalez-Alfonso et al., 2004).

our high signal-to-noise ratio only the $119\mu\text{m}$ line has been conclusively seen at all, in absorption (Colbert et al., *Ap.J.*, 511, 721, 1999). These differences in the OH lines reflect important differences in the molecular clouds that dominate in each of these various types of galaxies, and OH is a useful tool to distinguish these cloud properties – and the galaxies' morphologies.

We used two codes, a MonteCarlo code developed for SWAS (Ashby et al., *Ap.J.Lett.*, 539, L119, 2000) and a non-local code (Gonzalez-Alfonso and Chernicharo, *A&A*, 322, 938, 1997), as well as DUSTY (for the continuum), to calculate and cross-check line intensities and profiles in spherical clouds. The source is divided into a series of independent, concentric shells with adjustable temperatures, densities, abundances, etc.; microturbulence and/or radial velocity gradients are also included. The results confirm that the OH lines are often very optically thick (exceeding 100 in many cases). Since the critical densities for OH are high, above about 10^8cm^{-3} , the level populations are primarily determined by radiative effects.

From the analysis of this diverse set of sources and line strengths, several useful preliminary generalizations may be drawn. We tentatively conclude that galaxies can be grouped into three broad categories based solely on their OH line behavior. AGN: For NGC 1068, we model the clouds as being small, only a few pc in size, and dense. ULIGS: In Arp 220 the $34\mu\text{m}$ absorption confirms the OH maser radiative pumping mechanism (Skinner et al., *Nature*, 370, 117, 1997), and we find high OH column densities of about $2 \times 10^{17}\text{cm}^{-2}$. LIRGs: For galaxies like NGC 253 and Mkn 231, which have differing combinations of both emission and absorption lines, we typically find that the clouds are much larger, 10-100pc, and less dense. We have made substantial progress in the analyses, and future velocity-resolved spectra will enable even more refinements. Sensitive OH measurements should help categorize those sources whose morphology is otherwise ambiguous.

The far-infrared spectrum of Arp 220¹

Eduardo González-Alfonso^{2,3}

Universidad de Alcalá de Henares, Departamento de Física, Campus Universitario, E-28871 Alcalá de Henares, Madrid, Spain

eduardo.gonzalez@uah.es

Howard A. Smith

Harvard-Smithsonian Center for Astrophysics, 60 Garden Street, Cambridge, MA 02138

hsmith@cfa.harvard.edu

Jacqueline Fischer

Naval Research Laboratory, Remote Sensing Division, Code 7213, Washington, DC 20375

jackie.fischer@nrl.navy.mil

and

José Cernicharo

CSIC, IEM, Dpto. Astrofísica Molecular e Infrarroja, Serrano 123, E-28006 Madrid, Spain

cerni@damir.iem.csic.es

ABSTRACT

ISO/LWS grating observations of the ultraluminous infrared galaxy Arp 220 shows absorption in molecular lines of OH, H₂O, CH, NH, and NH₃, as well as in the [O I] 63 μm line and emission in the [C II] 158 μm line. We have modeled the continuum and the emission/absorption of all observed features by means of a non-local radiative transfer code. The continuum from 25 to 1300 μm is modeled **AS A WARM (106 K) NUCLEAR REGION THAT IS OPTICALLY THICK IN THE FAR-INFRARED**, attenuated by an extended region (size 2'') that is heated mainly through absorption of nuclear infrared radiation. *The molecular* absorption in the nuclear region is characterized by high excitation due to the high infrared radiation density. The OH column densities are high toward the nucleus ($2 - 6 \times 10^{17} \text{ cm}^{-2}$) and the extended region ($\sim 2 \times 10^{17} \text{ cm}^{-2}$). The H₂O column density is also high toward the nucleus ($2 - 10 \times 10^{17} \text{ cm}^{-2}$) and lower in the extended region. The column densities *in a halo that accounts for* the absorption by the lowest lying levels are similar to what are found in the diffuse clouds toward **the star forming regions in the Sgr B2 molecular cloud complex** near the Galactic Center. Most **notable** are the high column densities found for NH and NH₃ toward the nucleus, with values of $\sim 1.5 \times 10^{16} \text{ cm}^{-2}$ and $\sim 3 \times 10^{16} \text{ cm}^{-2}$, respectively, whereas the NH₂ column density is lower than $\sim 2 \times 10^{15} \text{ cm}^{-2}$. A combination of *PDRs in the extended region and hot cores with enhanced H₂O photodissociation and a possible shock contribution in the nuclei* may explain the relative column densities of OH and H₂O, whereas the nitrogen chemistry may be strongly affected by cosmic ray ionization. *The [C II] 158 μm line is well reproduced by our models and its "deficit" relative to the CII/FIR ratio in normal and starburst galaxies is suggested to be mainly a consequence of the dominant non-PDR component of far-infrared radiation, ALTHOUGH OUR MODELS ALONE CANNOT RULE OUT EXTINCTION EFFECTS IN THE NUCLEI.*

1. Introduction

With a redshift of $z = 0.018$, **Arp 220 (IC 4553/4)** is the nearest and one of the best studied ultraluminous infrared galaxies (ULIRGs). The tails observed in the optical, together with the double highly-obscured and compact ($0''.3$) nuclei observed in the near and mid-infrared, as well as in the millimeter, strongly suggest that the enormous luminosity of Arp 220, $\sim 10^{12} L_{\odot}$, is the result of galactic merging. Nevertheless, the concrete physical process responsible is still a matter of debate: the proposed sources are hidden active nuclei and/or bursts of star formation.

Molecular observations of Arp 220 provide unique clues to the physical and chemical processes occurring in the nuclei and their surroundings. In the millimeter region, CO observations have been carried out with increasingly high angular resolution (Radford, Solomon, & Downes 1991; Scoville et al. 1991; Okumura et al. 1994; Scoville, Yun, & Bryant 1997; Sakamoto et al. 1999). In particular they have shown that, on the one hand, CO emission arises from a region significantly more extended than the nuclei ($\sim 3 - 4''$), and on the other hand that the CO(2-1) to CO(1-0) intensity ratio is lower than 1, thus suggesting that CO mainly traces low density regions ($< 10^3 \text{ cm}^{-3}$). Observations of molecules with high dipole moment, like CS and HCN, have revealed that the fraction of molecular gas contained in dense clouds ($n(\text{H}_2) \geq 10^4 \text{ cm}^{-3}$) is much larger than in normal galaxies, yielding $\sim 10^{10} M_{\odot}$ of dense gas (Solomon, Radford, & Downes 1990; Solomon, Downes, & Radford 1992). Radford et al. (1991b) found that HCN(1-0) and $\text{HCO}^+(1-0)$ peak strongly toward the nuclei, but also show low-level extended emission. More recently, Aalto et al. (2002) have detected emission from the high density tracers HNC and CN, and the relatively low HCN/CN and HCN/HNC intensity ratios were attributed to widespread PDR chemistry.

¹Based on observations with the Infrared Space Observatory, an ESA project with instruments funded by ESA Member States (especially the principal investigator countries: France, Germany, Netherlands, and the United Kingdom) and with the participation of ISAS and NASA.

²Visiting Astronomer, Harvard-Smithsonian Center for Astrophysics, 60 Garden Street, Cambridge, MA 02138.

³CSIC, IEM, Dpto. Astrofísica Molecular e Infrarroja, Serrano 123, E-28006 Madrid, Spain.

The launch of the Infrared Space Observatory (ISO) opened a new window for the study of the physical and chemical properties of ultraluminous infrared galaxies. Despite the lack of angular and spectral resolution, the observations of Arp 220's far-infrared spectrum from 40 to 200 μm (Fischer et al. 1997, 1999) and of a number of individual lines in the SWS range (Sturm et al. 1996) provided new insights in our understanding of the ionic, atomic and molecular content of the galaxy. These wavelength regions are of great interest, because the bulk of the enormous luminosity is emitted in the far-infrared, and also because they contain lines of interesting molecular species. Skinner et al. (1997) reported the detection of the 35 μm OH line in Arp 220. Fischer et al. (1997, 1999) found that the far-infrared molecular absorption lines of OH, H_2O , CH, and NH_3 are significantly stronger in Arp 220 than in less luminous infrared-bright galaxies while the fine structure lines from ionic species are, to the contrary, extremely weak. Luhman et al. (1998, 2003) found that, relative to the far-infrared luminosity, the [C II] in ULIRGs is typically nearly an order of magnitude weaker than in lower luminosity infrared-bright galaxies. Sturm et al. (1996) reported the detection of two ortho- H_2 pure rotational lines, indicating that high masses of gas are subject to PDR conditions and/or shock activity.

The physical and chemical processes that account for the rich molecular far-infrared spectrum of Arp 220 can be better understood if quantitative values of the column densities of the above species, as well as their excitation conditions, are estimated. The presence of OH and, to some extent, of H_2O , may be indicative of PDR and/or diffuse interstellar cloud chemistry, and their column densities potentially give an estimate of the UV field in the source. On the other hand, large amounts of H_2O are produced in non-dissociative shocks (e.g. Cernicharo et al. 1999), where the OH abundance is also enhanced (Watson et al. 1985). The OH abundance is expected to be generally higher than that of H_2O in fast dissociative shocks (Neufeld & Dalgarno 1989). H_2O ice in grain mantles may also efficiently return to the gas phase through sublimation of mantles in "hot core" regions. But whatever the characteristics of the regions producing the observed

molecular features, the lines under study lie at wavelengths where the enormous infrared continuum flux approaches its maximum, and the molecular excitation of high-dipole species should be strongly affected by absorption of continuum radiation. Hence any reliable estimation of molecular column densities require accurate models for the dust emission. Unfortunately ISO's lack of angular resolution forces us to rely on plausibility arguments in our assumptions about the regions where the different lines are formed; some of these are based on general requirements of excitation, and others on conclusions from observations of galactic sources. The main goal of this work is thus to shed light on the physical and chemical processes in Arp 220, based on detailed model fits of its continuum and far-infrared molecular/atomic line absorption and emission spectrum. We adopt a distance to Arp 220 of 72 Mpc (projected linear scale of 350 pc/arcsec, Graham et al. 1990). In section 2 we present the ISO/LWS observations; in section 3 we discuss the line **identifications**; section 4 is a **discussion of the models for the continuum emission**; section 5 presents the models for the molecular and atomic species; in section 6 we discuss the implications of the radiative transfer models, and section 7 summarizes our main results.

2. Observations

The full 43-197 μm spectrum of Arp 220, obtained with the LWS spectrometer (Clegg et al. 1996) on board ISO (Kessler et al. 1996) (TDT=27800202), was presented by Fischer et al. (1997, 1999). The grating spectral resolution is $\approx 0.3 \mu\text{m}$ in the 43-93 μm interval (detectors SW1-SW5), and of ≈ 0.6 in the 80-197 μm interval (detectors LW1-LW5), corresponding to $\Delta v \geq 10^3 \text{ km s}^{-1}$. The lines are thus not resolved in velocity. The beam size of $\approx 80''$ ensures that all the continuum and line emission/absorption from Arp 220 (CO size $< 4''$, Scoville et al. 1997, hereafter SYB97) lie within the ISO aperture.

The data we present here was reduced using version 9.1 of the **Off Line Processing (OLP) Pipeline system** which we found to produce a higher signal-to-noise spectrum than OLP 10.1. However, we adopted the continuum correction given by OLP version 10.1, which

typically gives absolute responsivity corrections with uncertainty factors ~ 3 times lower than are produced by version 9 (Tim Grundy, private communication). In order to obtain a smooth spectrum throughout the whole LWS range, shifting scale factors lower than 10% were applied to several detectors, except for detector SW1 (43-64 μm) for which the correction factor was of 15%. Thus we attribute a conservative uncertainty of 15% to the overall continuum level.

The LWS spectrum of Arp 220 is presented in Figure 1 together with identifications of the most prominent lines. Owing to transient effects, the fluxes of weak lines as observed in the forward and reverse scans were found to differ significantly in some wavelength ranges. In these cases, the scan that showed higher signal-to-noise /bf ratio, or the average if the ratio was similar, was used. Nevertheless, the reverse scan was selected if the line appeared close to the upper end of the detector, because transient effects are expected to be minimal there. In wavelength regions where two detectors' responses overlap, line fluxes were generally found to be consistent. The only exception was the $\text{H}_2\text{O } 3_{22} - 2_{11}$ line at 90 μm , which showed in LW1 a flux 60% weaker than in SW5. We adopted here the SW5 spectrum, but the flux of the above H_2O line should be considered highly uncertain. The subtraction of a baseline (see Fig. 1) added additional uncertainty to the line fluxes, particularly in cases of broad features presumably composed of several lines. With the exception of the $\text{H}_2\text{O } 3_{22} - 2_{11}$ line, we estimate a line flux uncertainty generally lower than 35%.

3. General results

OH and H₂O: The FIR spectrum of Arp 220 is dominated by lines of OH and H₂O that are observed in absorption, with the exception of the OH $\Pi_{1/2} 3/2 - 1/2$ emission line at 163.3 μm . Figure 2 shows the level diagram of OH, ortho-H₂O and para-H₂O, and indicates the lines detected in Arp 220. Lines with very different excitation requirements are observed throughout the spectrum. The OH lines $\Pi_{3/2} J = 9/2 - 7/2$ at 65 μm and $\Pi_{1/2} J = 7/2 - 5/2$ at 71 μm have lower levels at 290 K and 415 K above the ground state,

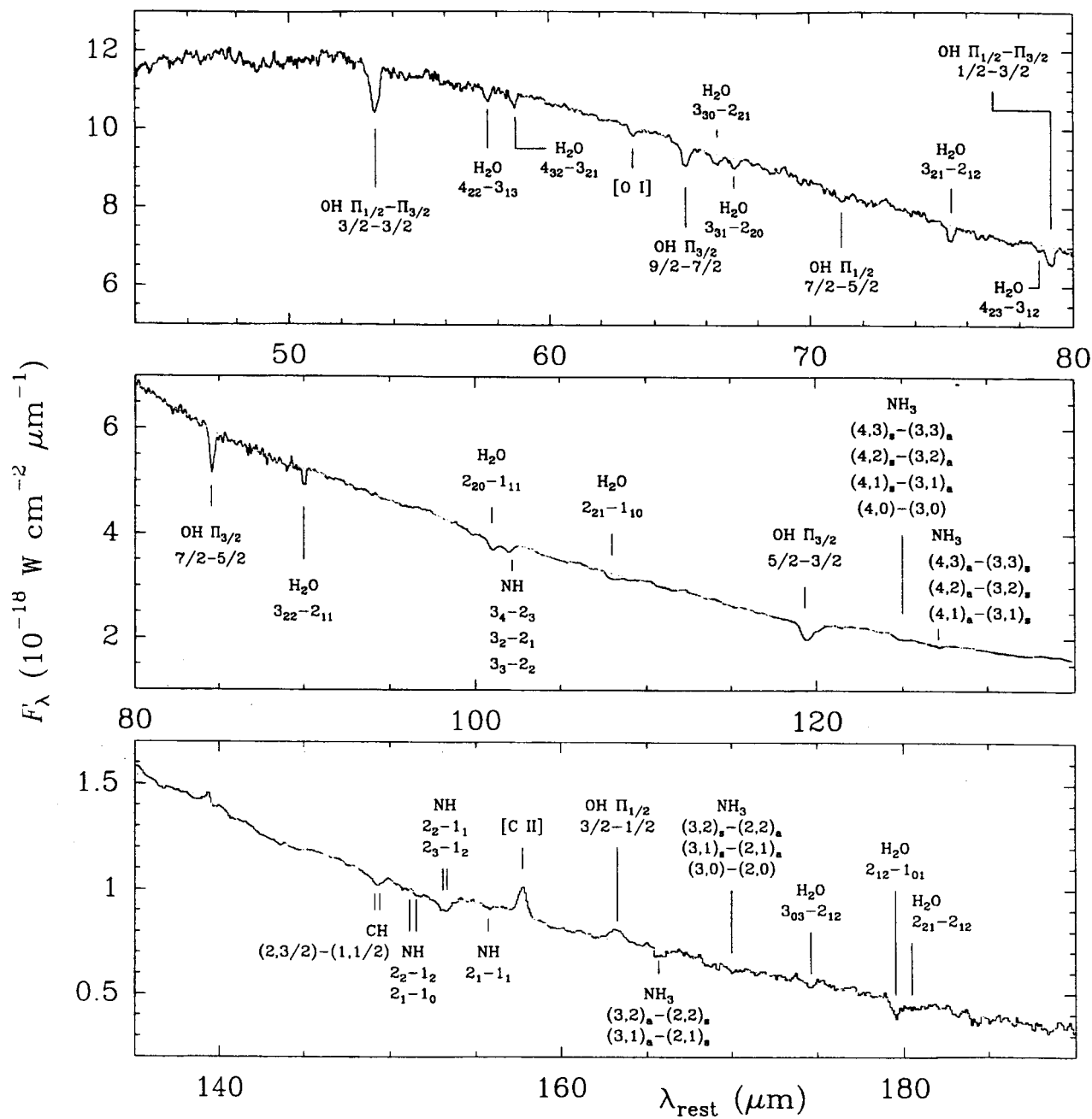


Fig. 1.— ISO/LWS spectrum of Arp 220, where the most prominent line features are identified (see text). The grey line shows the adopted baseline (continuum level).

respectively, whereas the H₂O lines 4₃₂ – 3₂₁ (59 μm) and 4₂₂ – 3₁₃ (58 μm) have lower levels at 305 K and 205 K. Strong absorption is also observed in the OH ground state lines at 53, 79, and 119 μm, as well as in the H₂O lowest-lying line at 179 μm. This wide range of **excitation suggests** that several regions with different physical conditions are contributing to the observed features (Fischer et al. 1999), and one of the goals of this work is to provide a reasonable estimate of the nature of these regions and their relative contributions to the spectrum. On the other hand, several of the lines have complex shapes, with evidence of shoulders suggestive of weaker secondary lines. In particular, the ground state OH 119 μm line shows a redshifted “shoulder”, which is detected in both the forward and reverse scans, although with somewhat different strengths. It could be attributed to the ¹⁸OH Π_{3/2} 5/2 – 3/2 line, although contamination by other species **such as CH⁺ cannot be ruled out**. Also, the redshifted “wing” of the H₂O 2₁₂ – 1₀₁ line at 179 μm, attributed in Fig. 1 to the H₂O 2₂₁ – 2₁₂ line, could also be contaminated by H₂¹⁸O, CH (see Fig. 7), and H₃O⁺.

CH and NH: The spectrum contains lines from other molecular species: like CH at 149 μm, NH₃ at 125, 166 and 170 μm and, very interestingly, strong absorptions at 102 and 153.2 μm that have been **identified as NH** in Fig 1. **Evidence for the latter identifications** is strengthened because of the presence of weak line-like features at 155.74 μm, and marginally at 151.53 μm, which would correspond to the NH 2₁ – 1₁ and 2₁ – 1₀ lines, respectively (see also Fig. 3). **Conceivably**, the line absorptions at 102 and 153.2 μm could be severely contaminated by other species, like C₃, H₂¹⁸O, NH₃, and even OH⁺. C₃ has a strong transition at 153.3 μm, but its contribution is expected to be minimal due to the lack of detection of other adjacent C₃ lines (in particular at 154.86 μm). The absorption at 102 μm may be contaminated by the H₂¹⁸O 2₂₀ – 1₁₁ line (just at 102.0 μm), but since the H₂¹⁸O should not be as strong as the corresponding adjacent line of the main isotope H₂¹⁶O, we regard this identification as also unlikely. Some contribution of NH₃ lines to the 102 μm feature might be expected, but they are somewhat shifted in wavelength (they lie between 101.5 and 101.7 μm). Both features could be

contaminated to some extent by OH⁺, with strong lines at 101.70 and 101.92 μm ($N_J = 3_3 - 2_2$ and $3_4 - 2_3$) and at 153.0 μm ($2_3 - 1_2$), but the strong absorption at 153.2 μm absorption could never be explained by OH⁺ alone. Therefore, despite the possible contamination from other molecules, NH is **probably** responsible for **most, if not all**, of the observed 153.2 μm absorption (see also Fig. 7). **Thus, although** the definitive assignment to NH **should await confirmation with** higher spectral resolution observations of the lowest-lying NH transitions at ~ 10³ GHz, we conclude that ISO observations strongly support its detection in Arp 220, and advance a model of the observed absorption (section 5) that can be useful to direct future observational and theoretical studies. If confirmed, this detection is the first extragalactic detection of NH, which has been previously detected only in galactic diffuse clouds through electronic transitions (Meyer & Roth 1991; Crawford & Williams 1997) and, interestingly, toward Sgr B2 in the Galactic Center **via** the same transitions detected in Arp 220 (Cernicharo, Goicoechea, & Caux 2000; Goicoechea, Rodríguez-Fernández, & Cernicharo 2004, hereafter GRC04).

NH₃: The spectrum of Arp 220 around 125 and 170 μm, shown in Figure 4, strongly supports the identification of NH₃. The shape of the 165.7 μm feature indicates transient effects, but the line is detected in both the forward and reverse scans. Some H₂O lines may contribute to the observed 125 and 127 μm features, but they are shifted in wavelength relative to the strongest absorption. This is the first extragalactic detection of infrared NH₃ lines. **With the detection of NH and NH₃ we might expect to detect NH₂**, but there is no evidence for its **strongest expected lines** at 159.5, 117.8 and 104.9 μm.

CO?: **An apparent emission line, detected in both the forward and reverse scans, is present at 173.7 μm in Fig. 1.** It coincides rather well with the expected position of the CO $J = 15 - 14$ line at 173.63 μm. **This identification cannot be confirmed by the detection of other expected CO lines because the CO $J = 14 - 13$ line at 186.0 μm lies at the noisy edge of the LW5 detector and the CO $J = 16 - 15$ line at 162.8 μm is blended with the OH 163.3 μm line.** The higher J lines are expected to be too weak to be detectable, given

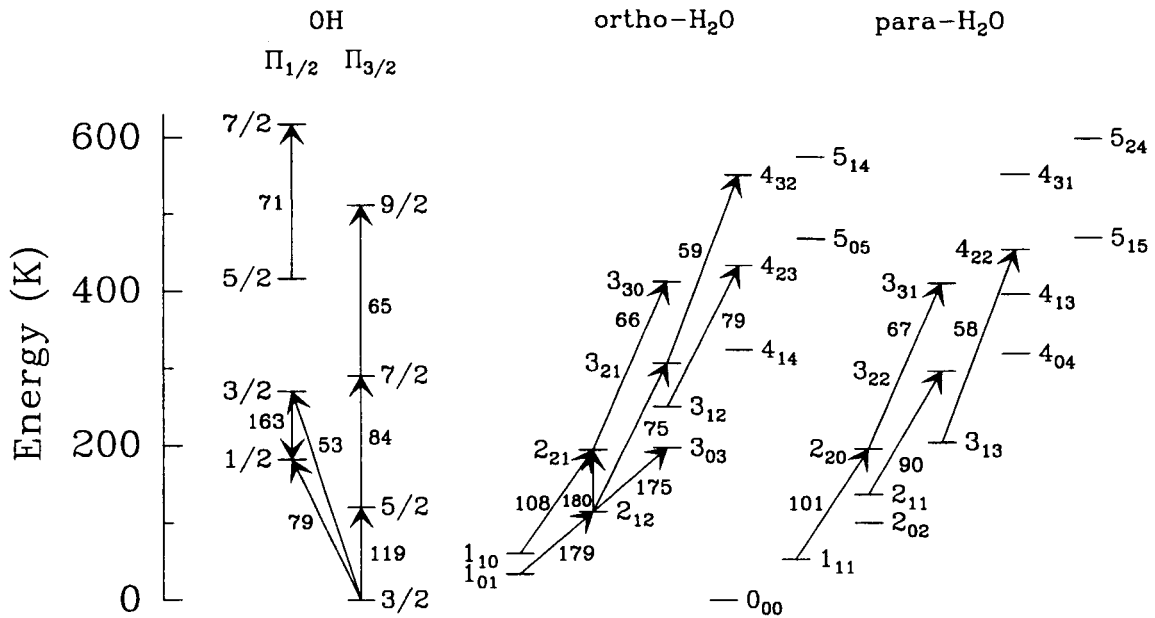


Fig. 2.— Energy level diagrams of OH and H₂O (ortho and para). Rotational levels with energies above the ground state up to 620 K are shown; the lines detected in Arp 220 are indicated with arrows and their wavelengths are in μm . OH Λ -doubling is ignored because the Λ -doublets are not resolved with the ISO grating resolution.

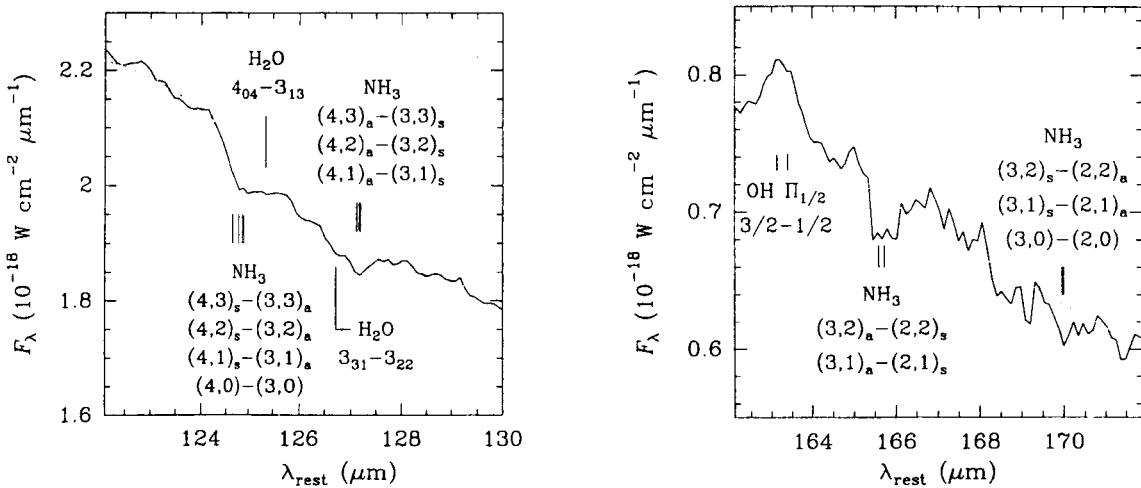


Fig. 4.— NH₃ lines around 125, 127, 166, and 170 μm . The grey line shows the adopted continuum level. The 125 and 127 μm features could be partially contaminated by the labelled H₂O lines.

the observed strength of the 173.7 μm feature.

[O I] and [C II]: The ISO spectrum also shows the [O I] 63.2 μm line in absorption and the [C II] 157.7 μm line in emission. The [O I] 145.5 μm line is not detected. These lines, as observed in Arp 220 and other ULIRGs, have been discussed elsewhere (Fischer et al. 1997, 1999; Luhman et al. 1998, 2003). In section 5 we present a simple model of the Arp 220 spectrum that may shed some light on the peculiar behavior of these lines in Arp 220.

In summary, the far-infrared spectrum of Arp 220 shows molecular lines of OH, H₂O, CH, NH, and NH₃. The atomic lines of [O I] at 63 μm and [C II] at 158 μm are also detected. Lines of other species, like CO, H₃O⁺, CH⁺, and OH⁺, could also contaminate the observed features, but our limited spectral resolution prevents the possibility of unambiguous detection. Only the [C II] 158 μm and the OH $\Pi_{1/2} 3/2-1/2$ 163 μm lines are clearly observed in emission. Lines from ions that would trace H II regions and/or an AGN are absent.

4. Models for the continuum

Figure 1 shows that the continuum peaks around $\sim 40 - 50 \mu\text{m}$. The bulk of the continuum from Arp 220 is emitted by heated dust grains. At 1.3 millimeter wavelengths, Sakamoto et al. (1999) showed that the continuum arises almost exclusively from the nuclei, with an equivalent size of $\sim 0''.4$. On the other hand, Soifer et al. (1999, hereafter S99) have shown that the two nuclei also account for essentially all the continuum at 25 μm . Combining both observations, S99 proposed two alternative scenarios to explain the continuum emission of Arp 220 from far-infrared to millimeter wavelengths. Our models of the continuum emission are entirely based on these scenarios, which we have **examined and refined** quantitatively on the basis of our ISO 45-200 μm spectrum.

Model S₁: In the first scenario (hereafter S₁), it is assumed that the emission from the nuclei is not significantly attenuated at 25 μm by **foreground material**. We have simulated the emission from the nuclei as arising from a single nucleus with effective size of $0''.41$. With an effective dust temperature of 85 K, and optically thick emission in the submillimeter, the requirement that the fluxes

at 25 and 1300 μm arise from the nuclei is fulfilled. However, the emission at 60-100 μm , as well as the total luminosity from the galaxy, are then underestimated and a more extended region (hereafter ER) must be invoked to account for the remaining flux. We identify this surrounding environment with the extended emission observed in CO, HCN, and HCO⁺. In this first scenario, then, most of the Arp 220 luminosity is produced in the ER, which has been modeled as a thin disk by SYB97, and as a warped disk by Eckart & Downes (2001). **Significantly, if this model is correct, a spatially extended starburst, responsible for the bulk of the far-infrared luminosity is inferred.**

Our best fit to the continuum using model S₁ assumptions is presented in Figure 5a, with derived physical parameters listed in Table 1. In all models, uniform densities throughout the different components are assumed for simplicity. In Table 1, λ_t is the wavelength for which the nucleus becomes optically thin ($\tau = 1$); owing to the **high opacities involved**, the inferred emission is rather insensitive to the spectral index β . Thus we have given values of the physical parameters for $\beta = 1.5$ and $\beta = 2$. The dust mass has been derived by assuming a mass-opacity coefficient of 12 cm²/gr (Hildebrand 1983). The parameters that have been allowed to vary in our models of the ER are the dust temperature T_d , the diameter d (within the range 500–800 pc), and the dust opacity; β is fixed to 2 to ensure negligible emission at millimeter wavelengths (see S99).

Model S₂: In the second scenario (hereafter S₂), the emission from the nuclei at 25 μm is assumed to be attenuated by foreground local dust with $\tau_{\text{abs}}(24.5 \mu\text{m}) = 1.2$, **a value which was chosen to be compatible with the silicate absorption observed in S99.** The nuclei account for the required flux at 24.5 and 1300 μm with $T_d \approx 106$ K, **significantly warmer than the ~ 85 K temperature in S₁ and, as before, the emission in the submillimeter is optically thick** (see Table 1). In this scenario as well, however, the flux at **60 – 100 microns** is again underestimated, and an emitting ER must also be involved to account for it. Nevertheless, the luminosity from the warm nuclei in S₂ is enough to account for the observed total luminosity from Arp 220, so that the ER merely re-radiates the emis-

sion from the nuclei and no extended starburst is then needed to provide the bulk of the luminosity.

Figure 5b shows our best fit for S_2 . The unique parameters that have been allowed to vary in our models of the ER are the diameter d and the dust opacity; β is again fixed to 2, and the dust temperature T_d (shown in the insert panel of Figure 5b) has been computed from the requirement that the heating balance the cooling throughout the source. We have assumed spherical symmetry with the nucleus, **the primary heating source**, located at the center of the ER, which is divided into a set of spherical shells to account for the variation of T_d with the distance to the nucleus. Despite the good fit to the continuum in Fig. 5b, S_2 **implicitly supposes a lack of spherical symmetry or some clumpiness**, because the derived radial opacity of the ER at $24.5 \mu\text{m}$ is 11.3, whereas the adopted opacity of the absorbing shell in front of the nuclei is $\tau_{\text{abs}}(24.5 \mu\text{m}) = 1.2$. Therefore these results should be considered **approximate, but suggestive**. The intrinsic geometry that underlies S_2 implies that the total luminosity, which coincides with the **luminosity of the nuclei**, is lower than the value inferred in S_1 , where spherical symmetry **and uniformity** is assumed for each component (Table 1).

Table 1 shows that $\beta = 2$ yields a dust mass of $\sim 10^8 M_\odot$ for the nucleus, and that S_1 gives a mass 1.4 times higher than S_2 . Since SYB97 infer a dynamical mass of $6 - 8 \times 10^9 M_\odot$ enclosed in the inner 250 pc radius, and this region contains the nuclei and most of the inner disk (the ER), S_2 with $\beta = 1.5$ is favoured in our models provided that the gas-to-dust mass ratio is not lower than the standard value of ≈ 100 .

It is worth noting that these models may be applied to the source as a whole, as implicitly assumed above, or alternatively to each one of an ensemble of N_c smaller clouds of radius R_c that do not spatially overlap along the line of sight. **The value of $N_c \times R_c^2$ determines the absolute scale, and the radial opacity and temperature distribution of each cloud as a function of the normalized radial coordinate, R_c , determine the continuum shape. Identical results are found as long as the above parameters remain constant.** Furthermore, both alternatives give identical total masses, but differ in the inferred mean **density, which scales as**

$\sqrt{N_c}$. $N_c = 1$ gives the lowest mean density $< n(\text{H}_2) >$, which is listed in Table 1. Typical values of a few $\times 10^4 \text{ cm}^{-3}$ are derived for the nuclei, accounting for the emission from molecules with high dipole moment **such as HCN, HCO⁺, HC₃N and CN** (see also SYB97). For the ER we obtain $n(\text{H}_2) < 10^3 \text{ cm}^{-3}$; since HCN and HCO⁺ appear to show extended low-level emission (Radford et al. 1991b), it is suggested that the actual density is higher than this lower limit or that the gas is clumpy.

Although both scenarios S_1 and S_2 reproduce the continuum emission from Arp 220 over the 25-1300 μm interval and support the constraints on the nuclear sizes derived from the available high angular resolution continuum measurements, the dynamical masses inferred from CO millimeter line observations favour S_2 with $\beta = 1.5$ for the nuclei. Moreover, as we discuss in sections 5.3 and 6.1, the observed line absorption/emission also favours model S_2 . We thus adopt scenario S_2 for the detailed modeling and analysis of the line emission and absorption.

4.1. Extinction

In both scenarios, the high brightness and compactness of the nuclei imply extreme **continuum optical depth**, corresponding to $A_V \sim 10^4$ mag. This conclusion is in strong contrast with the much more moderate values derived from *infrared and radio* hydrogen recombination lines (Genzel et al. 1998; Anantharamaiah et al. 2000). The high extinction derived here is the direct result of the measured 1.3 mm continuum flux from the nuclei, 210 mJy (Carico et al. 1992; Sakamoto et al. 1999), and the observed upper limit of the corresponding source size, $\sim 0''.4$ (Sakamoto et al. 1999). These values imply $\tau_d^{1.3\text{mm}} \times T_d(\text{K}) \sim 40$, which shows that even assuming unexpectedly high average dust temperatures (e.g. $T_d = 200 \text{ K}$) and $\beta = 1$ the dust emission is still optically thick even at $200 \mu\text{m}$. *On the other hand, the radio recombination lines observed by Anantharamaiah et al. (2000) are not affected by dust obscuration, although their predicted fluxes and the derived extinction may be somewhat model dependent.* These very different extinction values may be **understood** if we assume that the observed H recombination lines, tracing primarily *star formation, are formed in the outermost regions of the nu-*

TABLE 1
PHYSICAL PARAMETERS DERIVED FROM THE CONTINUUM EMISSION

Scenario	Component *	τ_{abs} (24.5 μm)	d (pc)	β	T_d (K)	λ_t (μm)	M_d (M_\odot)	$\langle n(\text{H}_2) \rangle^a$ (cm^{-3})	L (L_\odot)
S ₁	Nucleus	0	145	1.5	85	640	5.1×10^7	6.5×10^4	4.8×10^{11}
				2.0	85	770	1.3×10^8	1.6×10^5	4.8×10^{11}
S ₁	ER	0	630	2.0	50	110	5.2×10^7	8.1×10^2	8.3×10^{11}
S ₂	Nucleus	1.2	145	1.5	106	520	3.6×10^7	4.6×10^4	9.8×10^{11}
				2.0	106	650	9.3×10^7	1.2×10^5	9.8×10^{11}
S ₂	ER	0	660	2.0	40-90 ^b	82	3.9×10^7	5.3×10^2	—

^a Assuming a single source instead of an ensemble of clouds

^b The temperature is calculated throughout the ER from the balance between heating and cooling with the nucleus as the primary heating source

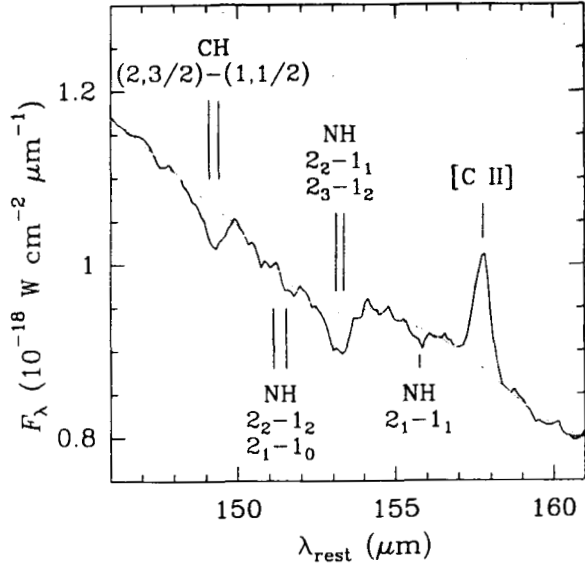


Fig. 3.— Line assignments in the vicinity of the 153.2 μm feature. The grey line shows the adopted continuum level.

clei, while a buried central energy source, responsible for the heating of dust in the innermost regions of the nuclei and a significant fraction of the galactic luminosity, is weak in recombination lines. If weak in recombination lines, the buried energy source is presumably weak in PAH features and PDR lines as well, consistent with the strong [C II] deficit in Arp 220 (see also section 5). Dust-bounded ionized regions, in which most of the Lyman continuum from nuclear starbursts or AGN is absorbed by dust rather than by gas, may explain these properties of Arp 220, as was proposed by Luhman et al. (2003). We further argue that the Lyman continuum luminosities derived from recombination lines do not empirically rule out the possibility that an AGN accounts for more than $\sim 50\%$ of the bolometric luminosity of Arp 220, because of the high dispersion of $L_{\text{bol}}/L_{\text{Lyc}}$ values shown by both starburst galaxies and AGN, the range of L_{Lyc} values derived from different tracers in Arp 220, AND THE UNCERTAINTIES IN THE ASSUMED EXTINCTION LAW AND THE DERIVED EXTINCTION (Genzel et al. 1998). Our derived $N(\text{H}_2) \sim 10^{25} \text{ cm}^{-2}$ is high enough to obscure a source of high 5–10 keV luminosity from one or both nuclei in Arp 220, so that a hidden AGN is allowed despite the relatively weak X-ray luminosity observed in Arp 220 (Clements et al. 2002). Haas et al. (2001) have also argued that a hidden AGN powers much of the luminosity of Arp 220 on the basis of the ob-

served submillimeter continuum excess relative to the $7.7 \mu\text{m}$ PAH flux.

5. Models for molecules and atoms

5.1. Comparison with Sgr B2

The comparison of the spectrum of Arp 220 with that of some well-studied galactic sources provides important clues about the regions where the observed lines are formed, while emphasizing the unique features that characterize the extragalactic source. In this sense, Sgr B2 (component M) is an ideal comparison source, just because it shares **common properties with Arp 220 despite the obvious differences in spatial scale** (and indeed possibly in nature). Figure 6 shows the continuum-normalized spectra of Sgr B2 (M) (kindly provided by J.R. Goicoechea) and Arp 220. Sgr B2 harbors newly born OB stars, ultracompact H II regions, and hot cores, enshrined in a dusty envelope which is heated by shocks and by radiation, and which radiates a high IR luminosity (see GRC04 and references therein). The envelope has the highest extinction in the direction of the N- and M-condensations, with optically thick emission in the far-infrared up to $\sim 200 \mu\text{m}$, and with foreground absorption lines of OH, H₂O, CH, and [O I] observed with the ISO/LWS grating (GRC04, Fig. 6). Fabry-Perot observations of Sgr B2 have also allowed the detection of other molecular species like NH, NH₃, NH₂, HD, H₃O⁺, and C₃, as well as high excitation lines of OH and H₂O (GRC04 and references therein). As shown above (section 4), the extinction toward the nuclei of Arp 220 is also very high, although the dust is significantly warmer than in the Sgr B2 envelope. The comparison between both sources is meaningful (at least as a first approximation, and from the point of view of the radiative transfer) as long as the nuclear region of Arp 220 can be considered an ensemble of continuum-thick molecular-rich clouds **such as Sgr B2**. For an ensemble of Sgr B2-like cloud, since both the continuum and the line absorption scale with the number of clouds, the *continuum-normalized* spectrum is the same as that of one individual cloud. This result applies even if the lines in the ensemble are broadened relative to the one-cloud emission due to cloud-to-cloud velocity dispersion and rotation, provided that the lines remain unresolved with the

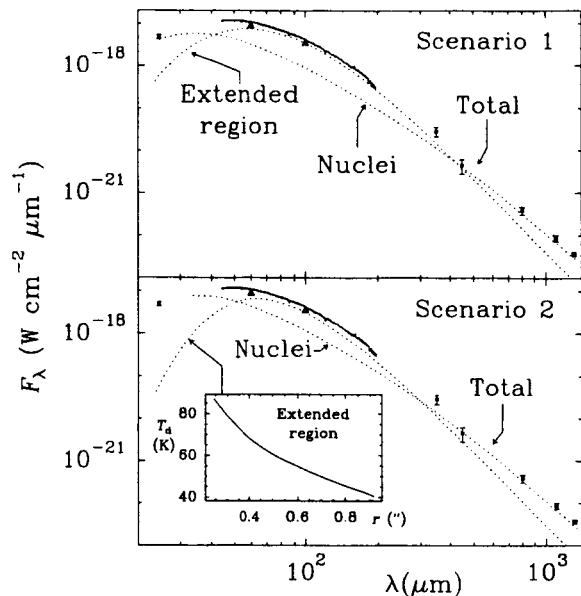


Fig. 5.— Fits of the continuum emission from Arp 220 in the 25–1300 μm range for scenarios (a) S₁ and (b) S₂. Solid line shows ISO-LWS spectrum of Arp 220, and filled triangles show the 60 and 100 μm IRAS fluxes for comparison. Filled squares show the fluxes measured by Soifer et al. (1999, 24.5 μm); Eales, Wynn-Williams, & Duncan (1989, 450 μm); Rigopoulou, Lawrence, & Rowan-Robinson (1996, 350, 800, and 1100 μm); and Sakamoto et al. (1999, 1300 μm). Dotted lines indicate the computed contributions from the nuclei and the ER, whereas the solid grey line shows the expected total flux. The insert panel shows the calculated dust temperatures in function of the radial angular distance for S₂ (see text).

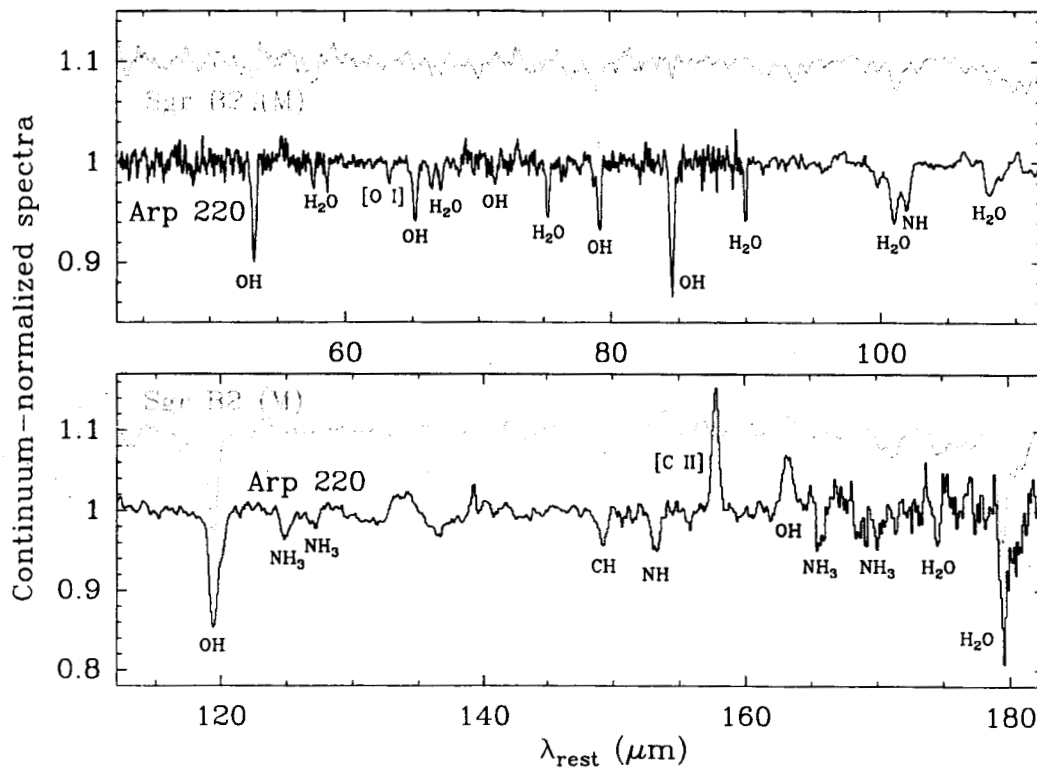


Fig. 6.— Continuum-normalized spectra of Sgr B2 (M) and Arp 220. The main carriers of some line features are indicated.

grating resolution. Thus the differences between the two spectra in Fig. 6 reveal real differences in excitation and/or column densities.

The high-excitation lines of OH and H₂O are much stronger in Arp 220 than in Sgr B2 (M) (see Fig. 6). In particular, the OH $\Pi_{3/2} J = 9/2 - 7/2$ 65 μm line, with strong absorption in Arp 220, is not detected in the grating spectrum of Sgr B2, and the OH $\Pi_{3/2} J = 7/2 - 5/2$ 84 μm line is also much weaker in Sgr B2 (M). This strongly indicates the presence in Arp 220 of a high excitation region with relatively high OH column densities. Fabry-Perot spectral resolution allowed Goicoechea & Cernicharo (2002) to detect high excitation OH lines in Sgr B2, and showed that they are pumped through absorption of far-infrared photons. **In Arp 220 also, these lines appear to be pumped by the strong infrared radiation flux in the neighbourhood of the nuclei (section 5.2).** Toward Sgr B2 (M), Goicoechea & Cernicharo (2002) derived $N(\text{OH}) \approx 2 \times 10^{16} \text{ cm}^{-2}$, and we may expect significantly higher column densities toward the nuclei of Arp 220. The peculiarity of Arp 220 is also revealed by the relatively strong absorptions in the NH₃ and NH lines. These species have also been detected toward Sgr B2 (M) with Fabry-Perot spectral resolution (Ceccarelli et al. 2002, GRC04), but Fig. 6 indicates much higher column densities in Arp 220, at least toward the nuclei.

GRC04 found that the OH $\Pi_{1/2} J = 3/2 - 1/2$ 163 μm line, pumped through absorption of photons in the OH $\Pi_{1/2} - \Pi_{3/2} J = 3/2 - 3/2$ 53.3 μm line, shows emission over a large region associated with Sgr B2. In Arp 220 the line is strong, suggesting significant widespread emission, i.e. from the ER. It is also worth noting that, although the [C II] line is not detected in the grating spectrum of Sgr B2 (M), Fabry-Perot observations allowed its detection (Vastel et al. 2002, GRC04), with a flux of $\approx 1.5 \times 10^{-17} \text{ W cm}^{-2}$ **for the component observed in emission. This value is, within a factor of 2, similar to strengths in the surrounding region where the continuum is however much weaker (GRC04). Therefore, in addition to effects of self-absorption and absorption of the continuum by C⁺ in foreground excitation clouds (Vastel et al. 2002, GRC04), the low [C II]/FIR ratio at Sgr B2 (M) is due to a strong increase in the**

FIR emission that is not accompanied by a corresponding rise of PDR line emission. Dust-bounded ionized regions (Luhman et al. 2003), together with extinction effects in the far-infrared, might account for the lack of PDR line emission associated with this additional infrared component. This is similar to our hypothesis for Arp 220's nuclei (section 5.6). The [C II] emission in Arp 220 is expected to arise from PDRs in the ER, where the bulk of the PAH emission is found (Soifer et al. 2002). As shown in Fig. 5, the ER dominates the observed far-infrared emission, but since the main heating sources are, according to model S₂, the nuclei, the ER is mainly heated via absorption of infrared rather than UV photons, its intrinsic luminosity is relatively low, and hence the [C II] line remains weak (section 5.6).

Finally, we stress that Arp 220 and Sgr B2 (M) show similar absorptions in the ground-state lines of OH and H₂O, as well as in the CH line at 149 μm . Fabry-Perot observations of the low-lying OH and H₂O lines toward Sgr B2 (M) (Cernicharo et al. 1997, GRC04), indicate that most of these absorptions are produced in diffuse low-excitation clouds located along the line of sight to Sgr B2 but not physically associated with it. The similar absorptions found in Arp 220 strongly suggest that a **diffuse** medium is also present there. In fact we have found that the combination model of the nuclei and the ER that reproduces reasonably the high excitation OH and H₂O lines, fails to explain the strong absorptions in the lowest-lying OH and H₂O lines. The presence of an absorbing diffuse component is strengthened by the detection of CH at 149 μm , because most of the corresponding absorption toward Sgr B2, with strikingly similar strength, has been associated with translucent clouds (Stacey, Lugten, & Genzel 1987, GRC04). This component could also have an important effect on the observed [O I] 63 μm line: it is detected in absorption toward both **sources** and Baluteau et al. (1997) found that most of the absorption toward Sgr B2 could be produced by foreground gas in diffuse clouds. We will call this diffuse absorbing component "the halo"; the presence of such a halo in Arp 220 finds independent support in the outermost disk observed in the CO millimeter

lines by SYB97.

5.2. Outline of the models

The dust models described in section 4 set up the basis for the molecular calculations. These are carried out with the method described in González-Alfonso & Cernicharo (1997, 1999), which computes the statistical equilibrium populations of a given molecule by assuming spherical symmetry and line broadening caused by microturbulence and/or radial velocity gradients. In the present calculations we have assumed, for simplicity, pure microturbulent line broadening, but some tests showed that the inclusion of a radial velocity gradient hardly modified the results. Rotational motion, which is present around the nuclear region of Arp 220 (e.g. SYB97, Sakamoto et al. 1999; Downes & Solomon 1998), is not included. Nevertheless, we note that for an arbitrary-shaped source rotating with uniform angular velocity around any axis, any two arbitrary points within the source have no Doppler shift along their joining segment, and therefore the statistical equilibrium populations and emergent fluxes are identical to those computed by ignoring rotation. The inclusion of uniform rotation would only broaden the expected emergent line profiles, for which our ISO spectrum provides no information. In the more general case of non-uniform rotation, our models may be considered a first-order approximation. The assumption of spherical symmetry and our neglect of steep velocity gradients that may result from cloud-to-cloud velocity dispersion MAY be considered more critical.

Our non-local code accounts for radiative trapping in the molecular lines, collisional excitation, and excitation through absorption of photons emitted by dust. The dust parameters derived above for S₁ and S₂ are used in the calculations for molecules. As in the case of the continuum models, we have modeled the nucleus and the ER separately. This is required, in S₂, by the relatively low dust opacities of the ER toward the nucleus as compared with the radial opacity of the ER (see above), **and** involves inevitably an additional uncertainty.

Since the dust in the nucleus is very optically thick throughout the ISO wavelength range, model results are only sensitive to the molecular column densities in the most external parts of the nucleus.

It is therefore assumed that only in the external-most regions of the nucleus, where the infrared lines are formed, the molecular abundances are different from zero (see Goicoechea & Cernicharo 2002, for the case of Sgr B2). Since dust and molecules are assumed to be coexistent, extinction effects within the nucleus are implicitly taken into account; they place important constraints on the molecular abundances. We have adopted a molecular shell thickness of 2×10^{18} cm, which for a mean $n(\text{H}_2) = 4.6 \times 10^4 \text{ cm}^{-3}$ (in S₂) corresponds to $A_V \sim 50$ mag and $\tau(50 \mu\text{m}) \approx 0.3$. For lines around $50 \mu\text{m}$, the contribution to the absorption by molecules located deeper into the nucleus was checked in some tests to be relatively weak, due to both dust and molecular line optical depth effects. Foreground extinction in S₂ was also taken into account. In the models for the ERs, which have much lower continuum opacities, we have assumed that dust and molecules have uniform abundance ratio throughout the whole region. The presence of the central nucleus is included in the calculation of the statistical equilibrium populations, but ignored in the calculation of the emergent fluxes to avoid accounting for it twice.

Toward the nucleus, absorption of continuum radiation determines the excitation of OH and H₂O; the radiative rates are much higher than the collisional ones even for molecular shock conditions ($n(\text{H}_2) = 5 \times 10^6 \text{ cm}^{-3}$ and $T_k = 300$ K). The rate coefficients of Offer, van Hemert, & van Dishoeck (1994) and Green, Maluendes, & McLean (1993) were used to check the collisional excitation of OH and H₂O, respectively. If molecular shocks were present, only **the absorption** of the lowest-lying lines would be significantly affected. Since **we use a halo** to match these lines, we cannot distinguish between shock and non-shock conditions (i.e., the line ratios are not sensitive to $n(\text{H}_2)$ and T_k within plausible values). For simplicity, physical parameters for the halo are derived by assuming non-shock conditions for the nucleus. Concerning the ER, widespread shock conditions are not applicable because they would involve strong emission in the H₂O 2₁₂ – 1₀₁ and 3₀₃ – 2₁₂ lines and in most OH lines (hard to cancel by any halo). Our molecular data are therefore only sensitive to the radial molecular column density N and the microturbulent velocity dispersion σ_v , so that only these two computational parame-

ters are required to define a model of a given component.

Similar to the dust models, models for molecules may be applied to the source as a whole, or alternatively to each one of an ensemble of smaller clouds that do not spatially overlap along the line of sight. Besides the scaling relationships pointed out above, the molecular column density must remain the same to obtain identical results when varying N_c . On the other hand, once the number of continuum sources N_c is fixed (e.g., $N_c = 1$), the same line fluxes are obtained if both N and σ_v are divided by the same factor f_c , and the resulting fluxes are then multiplied by f_c . The latter reflects the approximate equivalence between one absorbing cloud with column density N and velocity dispersion σ_v , and f_c clouds, with parameters N/f_c and σ_v/f_c , which overlap on the sky but not in the line-of-sight velocity space¹.

Variations in N and σ_v have different effects on the line absorptions. If σ_v decreases the absorptions are weaker for optically thick lines, but due to the increase of line opacities, the high-energy levels become more populated and the above weakness is more pronounced for the low-lying lines. On the other hand, the increase of N has little effect on very optically thick lines (most of them low-lying lines), but a larger effect on those with moderate opacities.

We have generated a grid of models for the nucleus and the ER of both S_1 and S_2 , by varying the above free parameters N and σ_v . In each model, the molecular shell is divided into a set of subshells in order to account for the spatial variation of the excitation temperatures of the lines. First we searched for the nucleus+ER combination model that best matches the OH and H₂O non-ground-state lines, with the same value of σ_v for both species. As pointed out above, the relatively deep absorptions of the OH and H₂O ground-state lines could not be fitted satisfactorily by any model, and a halo component was added to match these lines. The halo was assumed to be a purely absorbing shell; although the equilibrium populations were computed in spherical symmetry assuming a size of three times that of the ER,

¹In fact the models could be defined in terms of the two independent variables N/σ_v and $N \times f_c$; nevertheless we will use the variables N and σ_v with $f_c=1$.

limb emission (i.e. emission for impact parameters that do not cross the continuum source) was ignored in the calculation of the fluxes emergent from the halo.

Once the model for OH and H₂O is determined, models for the other detected species are performed, also keeping fixed the value of σ_v derived above for each component. Figure 7 compares the derived model spectrum and the observed one, and Table 2 lists the inferred parameters. The next sections are devoted to **explaining** the details of these calculations and results.

5.3. OH and H₂O

Our best model fits for the high excitation lines of OH and H₂O come from model S_2 , and the results presented here will focus on this scenario. The main difference between S_1 and S_2 consists in the higher column densities and/or broader line widths required by S_1 to reproduce the lines, owing to the fact that T_d is significantly lower in S_1 . Models for the nucleus with broad line widths ($\sigma_v > 60$ km s⁻¹, see below), however, predict strong absorptions in some OH and H₂O lines, such as the OH $\Pi_{1/2} J = 5/2 - 3/2$ 98 μ m and the H₂O $3_{13} - 2_{02}$ 138 μ m lines, which are not observed. Therefore S_2 , which still requires high column densities, is favoured by our models.

Our best model fits for the high excitation lines involve column densities of $2 - 6 \times 10^{17}$ cm⁻² for both OH and H₂O, and $\sigma_v = 50 - 30$ km s⁻¹, towards the nucleus. The model for the nucleus reproduces nearly the whole absorption in the OH $\Pi_{1/2} 7/2 - 5/2$ and $\Pi_{1/2} - \Pi_{3/2} 5/2 - 5/2$ lines, most of the OH $\Pi_{3/2} 9/2 - 7/2$, and significant absorption in the other lines **but by far too weak in the ground-state lines**. It also reproduces the full absorptions in the H₂O $4_{22} - 3_{13}$, $4_{32} - 3_{21}$, $3_{30} - 2_{21}$, $3_{31} - 2_{20}$, and $4_{23} - 3_{12}$ lines, and significant absorption in the $3_{21} - 2_{12}$ and others. The somewhat low value derived for σ_v is required to keep the absorptions weak in some low excitation lines which are marginally or not detected. Since low σ_v implies low velocity coverage for absorption of the continuum, the column densities that are needed to explain the absolute values of the absorptions in high excitation lines are relatively high. We stress that this value of σ_v must be interpreted as a strong lower limit on the linewidths that would be observed with high enough spectral

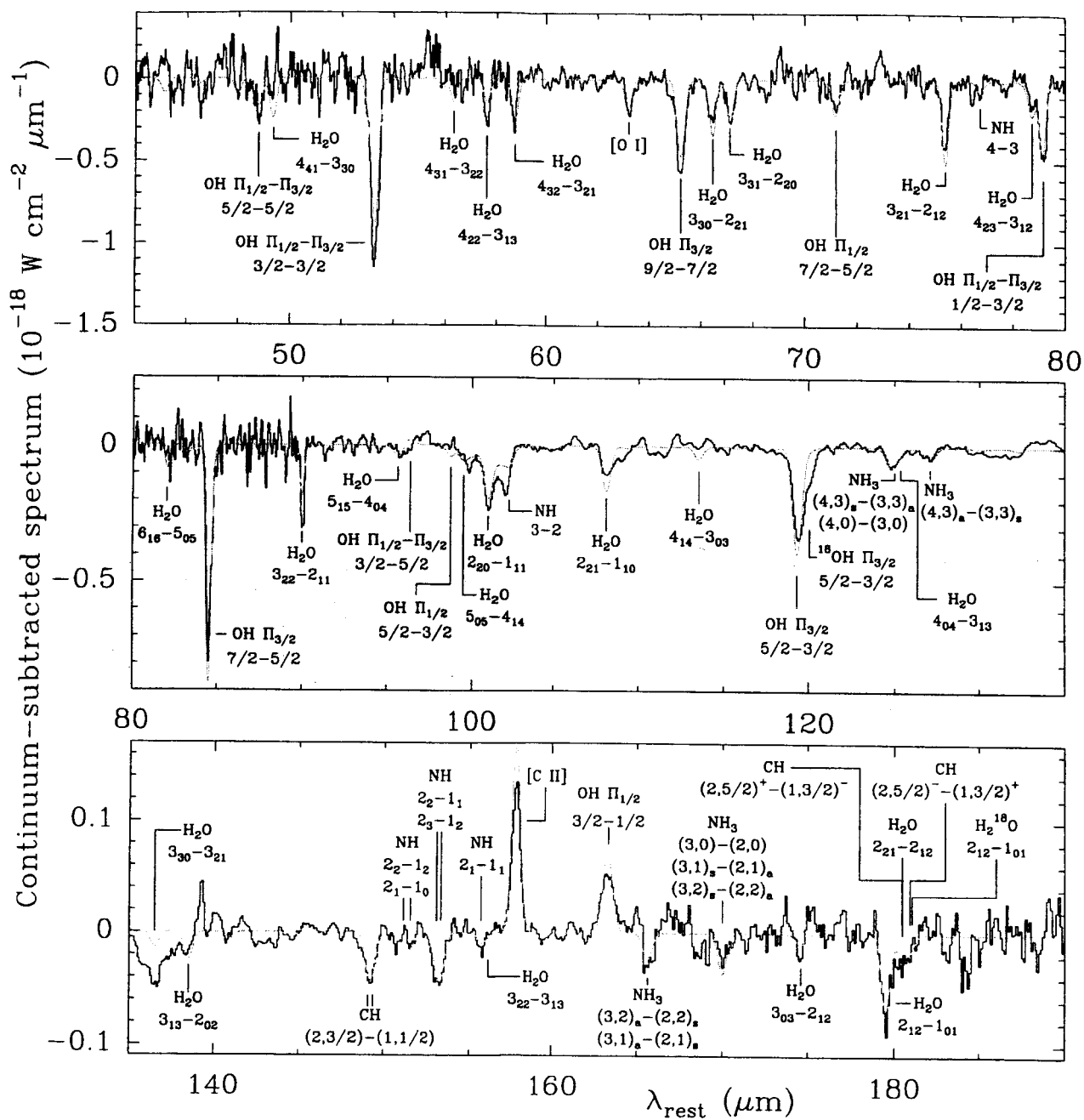


Fig. 7.— Continuum-subtracted spectrum of Arp 220, compared with the result of the model (in grey). The line features that contribute more to the model are identified (see text).

TABLE 2
COLUMN DENSITIES TOWARD ARP 220^a

Species	Nucleus	ER	Halo
OH	2.0×10^{17}	2.0×10^{17}	1.8×10^{16}
H ₂ O	2.0×10^{17}	3.0×10^{16}	1.5×10^{16}
CH	—	—	2.0×10^{15}
NH	1.3×10^{16}	—	1.8×10^{15}
NH ₃	2.8×10^{16}	—	4.0×10^{15}
C ⁺	2.0×10^{19}	2.0×10^{19}	—
O	5.0×10^{19}	5.0×10^{19}	2.7×10^{18}

^aUnits are cm⁻²

resolution, because rotation and cloud-to-cloud velocity dispersion would broaden the observed lines. The CO kinematic models of Arp 220 by SYB97 found a generic value of $\sigma_v = 90 \text{ km s}^{-1}$; as the authors discuss this value should be considered the **joint** effect of the local linewidth and the cloud-to-cloud velocity dispersion over a scale of ~ 100 pc. Our σ_v is the local linewidth involved in the calculation of opacities and directly related to the molecular excitation, and thus the kinematic value of SYB97 must be considered here an upper limit.

It is worth noting that the above column densities are derived by forcing the OH and H₂O high excitation lines to arise in the same region. A slight improvement to the fit of the H₂O lines is obtained with even lower σ_v , 25 km s^{-1} , and $N(\text{H}_2\text{O}) \sim 10^{18} \text{ cm}^{-2}$. This may indicate that H₂O and OH toward the nucleus do not arise in the same regions. We will adopt in the following the nucleus model with $\sigma_v = 50 \text{ km s}^{-1}$, corresponding to the spectrum shown in Fig. 7 and the parameters given in Table 2, and estimate an uncertainty of a factor of ~ 3 on the derived column densities.

Once the model for the nucleus is matched, a search of the combination ER+halo that better accounts for the remaining flux in non ground-state lines is searched for. The ER mainly accounts for the OH $\Pi_{1/2} 3/2 - 1/2$ $163 \mu\text{m}$ line, which is uniquely observed in emission (but predicted in absorption in the nuclei), for more than half of the absorption observed in the OH $\Pi_{3/2} 7/2 - 5/2$ line, for reemission in the $\Pi_{1/2} 5/2 - 3/2$, and for sig-

nificant absorption in the three ground-state OH lines. We estimate for the ER $N(\text{OH}) \sim 2 \times 10^{17} \text{ cm}^{-2}$, with $\sigma_v = 50 \text{ km s}^{-1}$ throughout most of the ER and $\sigma_v = 90 \text{ km s}^{-1}$ just around the nucleus. This higher value of σ_v was required to obtain significant reemission in the non-detected OH $\Pi_{3/2} 7/2 - 5/2$ line; since here geometrical effects may be important, this result should be considered with caution. For H₂O we obtain a significantly lower $N(\text{H}_2\text{O}) \sim 3 \times 10^{16} \text{ cm}^{-2}$, giving significant absorption in the $3_{21} - 3_{12}$, $2_{20} - 1_{11}$, and $2_{21} - 1_{10}$ lines, and some reemission in the $3_{03} - 2_{12}$ line. Since the halo also yields some absorption in these H₂O lines but much deeper absorption in the ground-state $2_{12} - 1_{01}$ one (see below), the relative H₂O column density in these components is not well determined.

In the halo, the values of $N(\text{OH})$ and σ_v were determined by fitting the missing absorption in the three OH ground-state lines. A value of σ_v , relatively low, $15\text{--}20 \text{ km s}^{-1}$, and $N(\text{OH}) \sim 2 \times 10^{16} \text{ cm}^{-2}$, were found to reasonably fit the fluxes of the 79 and $119 \mu\text{m}$ lines, though the flux of the $53 \mu\text{m}$ line is somewhat underestimated (Fig. 7). Higher values of σ_v would predict too much absorption in the already saturated $119 \mu\text{m}$ line. For H₂O we find $N(\text{H}_2\text{O}) \sim 1.5 \times 10^{16} \text{ cm}^{-2}$. Owing to the strong radiation field from the nucleus and ER, H₂O in the halo is still significantly excited, thus yielding also some absorption in the $2_{20} - 1_{11}$, $2_{21} - 1_{10}$ and $3_{03} - 2_{12}$ lines.

Despite the generally satisfactory fit obtained for the OH and H₂O lines, the shoulder of the

OH 119 μm line, presumably produced by the ^{18}OH $\Pi_{3/2}$ $5/2 - 3/2$ line, is not reproduced. The models assume $^{16}\text{OH}/^{18}\text{OH}=500$; however, the isotopic abundance ratio in Arp 220 required to reasonably fit the 120 μm shoulder is as low as $^{16}\text{OH}/^{18}\text{OH}\sim 50$. This value cannot be ruled out if ^{14}N is efficiently converted into ^{18}O in nuclear processing of high mass stars, and then efficiently ejected to the interstellar medium through stellar winds and/or supernovae (Henkel & Mauersberger 1993). Also, there is compelling evidence for isotopic ratios of 150–200 in starburst regions of nearby galaxies (Henkel & Mauersberger 1993). Due to the low spectral resolution of the spectrum, and the possibility that the feature is contaminated by other species, we do not attempt to place useful constraints on this ratio. Nevertheless, we conclude that a very low $^{16}\text{OH}/^{18}\text{OH}$ abundance ratio likely applies to Arp 220, perhaps indicating an advanced stage starburst (Henkel & Mauersberger 1993).

5.4. CH

We assume that the CH line we observe at 149.2 μm arises in the halo, based on the results obtained toward the Galactic Center (see GRC04). We derive $N(\text{CH})\approx 2 \times 10^{15} \text{ cm}^{-2}$ by fitting the feature. Unlike the case of Sgr B2, however, the far-infrared emission from the nuclear region of Arp 220 is so strong that significant excitation of the $(N, J)=(1, 3/2)$ rotational level occurs, and our models for the halo predict some contribution by CH to the absorption at 181 μm (Fig. 7). The latter is uncertain, however, because the feature at 181 μm could be contaminated by H_3O^+ (GRC04) and/or by stronger absorption of H_2^{18}O , whose abundance relative to H_2^{16}O could be enhanced relative to the assumed value of 1/500. On the other hand, there is a wing-like feature at 118.5 μm , observed in both the forward and reverse scans, which could be caused by the doublet CH $(3, 7/2)-(2, 5/2)$. If so, and since the excitation of this line requires a relatively strong radiation field, there would be CH in the nuclei that would account for about 1/3 of the absorption at 149.2 μm , and the CH column density in the halo would be 2/3 of the quoted value.

5.5. NH and NH_3

Assuming that the 153.2 μm absorption feature is caused entirely by NH, we have obtained $N(\text{NH})\sim 10^{16} \text{ cm}^{-2}$ toward the nucleus. The model reproduces the marginal absorption feature at 76.8 μm , attributable to the $N_J = 4_J - 3_J'$ lines. For the above column density, the $2_2 - 1_1$ and $2_3 - 1_2$ lines at 153.2 μm become saturated and the associated feature is not completely reproduced, so that we have added an additional halo component with $N(\text{NH})\approx 2 \times 10^{15} \text{ cm}^{-2}$ (Table 2). Nevertheless, this model still underestimates the absorption at 102 μm , strongly suggesting the contribution from other species (section 3).

Within a given K -ladder, the excitation of the NH_3 non-metastable levels is determined by absorption of far-infrared continuum photons, while the metastable levels in $K = 2, 3, \dots$ are pumped through collisions (see e.g. Ceccarelli et al. 2002, for the case of Sgr B2). In the model of Fig. 7 we have assumed an average density of $n(\text{H}_2)= 4.6 \times 10^4 \text{ cm}^{-3}$ and $T_k = 100 \text{ K}$, but we have checked that the model results are insensitive to the adopted T_k because of the blending of lines from different K -ladders to each spectral feature in our spectrum (Fig. 1). We obtain $N(\text{NH}_3)\sim 3 \times 10^{16} \text{ cm}^{-2}$ toward the nucleus to fit the absorptions at 125 and 127 μm (Fig. 7). Besides the absorption in the lines showed in Fig. 4, the model predicts significant absorption at $\approx 100 \mu\text{m}$ and $\approx 101.6 \mu\text{m}$, caused by $(J, K) = (5, K) - (4, K)$ lines. The model, however, fails to explain the strong absorption at 166 μm , and therefore an halo component with $N(\text{NH}_3)\sim 4 \times 10^{15} \text{ cm}^{-2}$ has been added to the global model of Fig. 7. Nevertheless, the halo components of NH and NH_3 should be considered uncertain, because variations in the background continuum associated with each component could in principle account for the missing flux in the lines.

Finally, we have explored the possibility that the NH_2 radical contributes to the spectrum at some wavelengths. The expected strongest absorption from NH_2 is found at $\approx 159.5 \mu\text{m}$, caused by the strongest components of the $3_{13} - 2_{02}$ ortho line (the hyperfine structure was neglected in these calculations, but the split of the levels due

to the unpaired electronic spin of 1/2 was taken into account). At this wavelength, a marginal absorption feature may be attributed to NH_2 , and is approximately fit with a model for the nucleus where $N(\text{NH}_2) \sim 10^{15} \text{ cm}^{-2}$. We have included this model of NH_2 in Fig. 7 to show that the expected absorption in other lines, like the $3_{22} - 2_{11}$ one at $105 \mu\text{m}$, do not conflict with the observations, and we conclude that $N(\text{NH}_2) \leq 2 \times 10^{15} \text{ cm}^{-2}$.

5.6. C II and O I

A crucial test of our model is whether it can reproduce the [C II] $157.7 \mu\text{m}$ emission and [O I] $63.3 \mu\text{m}$ absorption lines. Among ULIRGs, Arp 220 shows one of the most extreme [C II] deficits ($F_{\text{CII}}/F_{\text{FIR}} \approx 2 \times 10^{-4}$, Luhman et al. 2003). The [C II] line is formed within $A_V \leq 2$ mag from the surfaces of PDRs (e.g. Wolfire, Tielens, & Hollenbach 1990), where the UV field from nearby high mass stars, or from the average galactic field has not been significantly attenuated. In this region, photodissociation maintains most of the gas in atomic or singly ionized form, but some radicals, like OH and NH, find their maximum abundances there (Sternberg & Dalgarno 1995). In particular, OH is expected to be an excellent molecular tracer of PDRs' surfaces, given that its abundance is rather low in UV-shielded quiescent molecular clouds. Its abundance relative to H nuclei within the C^+ region of dense PDRs is expected to approach the value of $\sim 3 \times 10^{-6}$ (Sternberg & Dalgarno 1995). In fact, Goicoechea & Cernicharo (2002) have found an abundance of $\approx 2 \times 10^{-6}$ in Sgr B2, and it could be as high as 5×10^{-6} around the galactic center (Genzel et al. 1985). We have estimated $X(\text{OH}) \sim 1 - 3 \times 10^{-6}$ toward the nucleus of Arp 220.

On the above grounds, and adopting a gas phase carbon abundance of 1.4×10^{-4} (Savage & Sembach 1996), we assumed $N(\text{C}^+)/N(\text{OH})=100$ in Arp 220 (Table 2), and we computed the expected [C II] line emission by assuming excitation through collisions with H (Tielens & Hollenbach 1985). The collisional rates were taken from Launay & Roueff (1977a), and H densities of $5 \times 10^4 \text{ cm}^{-3}$ and 10^3 cm^{-3} were assumed for the nucleus and ER, respectively. Since the critical density is $3 \times 10^3 \text{ cm}^{-3}$ (Kaufman et al. 1999), results for the nucleus are not critically dependent on the as-

sumed density. They are also insensitive to the assumed temperature as long as it is higher than $\sim 100 \text{ K}$ (Wolfire et al. 1990). Thus our results are only sensitive to the assumed density in the ER, and to the assumed C^+ abundance.

The result of this calculation has also been added to the overall model of Fig. 7 ($T_k = 500 \text{ K}$ has been assumed), providing a reasonable fit to the [C II] line emission. The contribution from the nucleus is only 14% of that from the ER because of the low volume of the nuclear emitting region. The expected line flux from the nucleus **could be lower if absorption of the underlying continuum by low-excitation C^+ in the halo, ignored in this model, occurs** as observed in Sgr B2 (M) (GRC04). The bulk of the line emission arises from the ER. The situation toward Arp 220 resembles what is found in Sgr B2 (GRC04), where the line is emitted mainly from an extended region around condensations N and M, while the strong FIR source itself is not associated with corresponding observable [C II] line emission.

The [O I] $63.3 \mu\text{m}$ line has been modeled by assuming $N(\text{O I})/N(\text{OH})=250$ (Table 2); although the oxygen abundance is expected to be twice that of C^+ in the atomic region, it is expected that further atomic oxygen exists deeper into the clouds (Sternberg & Dalgarno 1995). For this reason, a wide range of excitation temperatures is expected for the [O I] line. We have just fitted a single "effective" kinetic temperature and assumed also collisions with atomic H. The same densities as assumed above for C^+ excitation are used for O I, and the collisional rates are taken from Launay & Roueff (1977b).

Our calculations show that absorption in the [O I] $63.3 \mu\text{m}$ line is obtained, both toward the nucleus and the ER, with an effective $T_k = 200 \text{ K}$, but the line is still too weak to account for the observed feature. Given the high O I abundances that are expected in diffuse clouds (Baluteau et al. 1997), we have added to the model a halo component with $N(\text{O I})=3 \times 10^{18} \text{ cm}^{-2}$ (Table 2). This model accounts for the observed absorption at $63.3 \mu\text{m}$ (Fig. 7).

On the basis of the low extinction derived from infrared and radio H recombination lines and the high optical depth derived from our dust models (section 4.1), and the assumption that [C II] emis-

sion is expected to suffer extinction similar to that of the recombination line emission, we infer that extinction does not play a role in the [C II] deficit and favor the explanation proposed by Luhman et al. (2003, see also section 5.1) that non-PDR far-infrared emission is responsible for the [C II] deficit in Arp 220. Nevertheless, our continuum models by themselves (section 4) cannot rule out the possible role of far-infrared extinction on the measured line fluxes: the derived high nuclear far-infrared opacities indicate that only the most external regions of the nuclei, where the OH and H₂O lines are formed, and the ER, are able to contribute to the [C II] line emission. Our model fits cannot discern whether the *intrinsic* nuclear [C II] emission is negligible or rather is obscured by dust. In either case, we have shown that the [C II] line is well reproduced by assuming that C⁺ and OH are coexistent.

6. Discussion

6.1. The Extended Region (“ER”)

Our models support the widespread presence of PDRs in the ER. Both the high OH and C II column densities indicate that the UV field from newly formed stars have a profound effect on the chemistry in the ER. Significant contributions from shocks can be neglected, as was pointed out in section 5.2. The H₂O-to-OH abundance ratio is significantly lower than 1, probably indicating enhanced H₂O photodissociation. Both the models for dust and the [C II] 158 μm line emission indicate rather moderate densities ($n_{\text{H}} \sim 10^3 \text{ cm}^{-3}$).

Our models also indicate that the bulk of the [C II] line emission arises in the ER. It is therefore likely that star formation is responsible for this emission. This result is strongly supported by the observations of Soifer et al. (2002), who found that the PAH emission is also spatially extended. Assuming a “normal” [C II]/FIR ratio, i.e. $F_{[\text{C II}]} / F_{\text{FIR}} = 5 \times 10^{-3}$ (Stacey et al. 1991), the expected intrinsic FIR emission from the ER is $\sim 3 \times 10^{10} L_{\odot}$, i.e. $\sim 3\%$ of the total galactic luminosity. This estimate supports the scenario S_2 that has been used to model the line emission. According to our models, the total FIR luminosity (due to absorption and re-emission of nuclear infrared radiation) from the ER is much higher than the intrinsic (PDR) emission. Our estimate of the

intrinsic ER luminosity is somewhat lower than that derived by Soifer et al. (2002) and Spoon et al. (2004), who found a lower limit of $\sim 7 \times 10^{10} L_{\odot}$, but confirms qualitatively their results. The starburst luminosity in the ER seems to be similar to that of moderately bright infrared galaxies, like NGC 253 (Radovich, Kahanpää, & Lemke 2001).

The warm mass in the ER derived from our OH models is $\sim 10^9 M_{\odot}$, assuming $X(\text{OH})=10^{-6}$ relative to H nuclei and the warm H₂ arises from the same volume as the OH. This estimate of mass may be considered an upper limit. From the H₂ rotational lines detected by ISO, Sturm et al. (1996) estimated $\sim 3 \times 10^9 M_{\odot}$ of warm gas. Given the uncertain correction by extinction, it is likely that an important fraction of the H₂ emission arises in the ER.

6.2. The halo

The models also indicate the presence of a halo. Despite the uncertainties in the column densities of this component, they are typical of those found toward our galactic nucleus: $N(\text{H}_2\text{O}, \text{OH}) \sim 2 \times 10^{16} \text{ cm}^{-2}$ have been also derived in the diffuse medium toward Sgr B2 (Cernicharo et al. 1997; Neufeld et al. 2003; Goicoechea & Cernicharo 2002), and the derived $N(\text{CH}) \approx 2 \times 10^{15} \text{ cm}^{-2}$ is also similar to that found toward Sgr B2 by GRC04 and Stacey et al. (1987). The column densities in the halo derived for NH and NH₃ are uncertain because they are based on single lines, but they could also exist in a population of molecular clouds located far away from the nuclear region.

6.3. The nuclei

The similarity of the OH column densities in the ER and the nucleus may suggest that, at least to some extent, we are observing the same widespread OH component, and that OH is more excited toward the nucleus because of the underlying stronger infrared continuum in that direction. On this ground a PDR origin of the observed OH would be favoured. However, the inferred high H₂O column density would be difficult to explain in this context. Although H₂O is expected to form efficiently in UV-shielded regions of dense PDRs (Sternberg & Dalgarno 1995), with total column densities similar to those of OH, there seems to be

no clear correlation between $N(\text{OH})$ and $N(\text{H}_2\text{O})$. In fact, the H_2O column density in the ER is significantly lower than that of OH. Also, detection of NH_3 and, above all, of NH, seem to indicate an additional **nuclear** component.

OH could also arise in C-shocks (Watson et al. 1985), but it is unlikely that they dominate the OH absorptions because $N(\text{H}_2\text{O})$ would then be at least one order of magnitude higher than $N(\text{OH})$. However, an interesting possibility is that those C-shocks, or alternatively hot core regions, are combined with PDRs, i.e., H_2O produced there is subject to a strong UV field and thus to photodissociation. This process may be enhanced if there is hot gas emitting X-rays, like in supernova remnants where the OH abundance is expected to be $\geq 10^{-6}$ (Wardle 1999), or from a nuclear AGN. In the nuclei of Arp 220, several compact 18 cm continuum sources indicate the presence of high luminous supernovae (Smith et al. 1998); however, the extended and **external** OH required to explain the infrared data suggests a more widespread component. The diffuse OH megamaser emission found in Arp 220 should be related to it (Lonsdale et al. 1998). Soft-extended and hard-compact X-ray emission, detected around and from the nuclei (Clements et al. 2002), could be responsible for photodissociation of H_2O produced in shocks and hot cores, thus enhancing the OH abundance. In particular, hot cores are expected to exist widely in the nuclei, given the high dust temperatures and densities found there. The presence of J-shocks, where $N(\text{OH})$ is expected to be higher than $N(\text{H}_2\text{O})$ except for high enough preshock densities (Neufeld & Dalgarno 1989), cannot be disregarded.

The high column densities obtained for NH and NH_3 seem to indicate that standard gas-phase PDR chemistry alone is not able to explain the full molecular data in Arp 220. Sternberg & Dalgarno (1995) predicted for a PDR an NH column density more than two orders of magnitude lower than that of OH, whereas we estimate $N(\text{OH})/N(\text{NH}) \sim 20$ in Arp 220. The enhancement of NH relative to OH **may be more** than one order of magnitude. In Sgr B2, GRC04 also found a somewhat high $N(\text{NH})$ relative to OH, i.e. $N(\text{OH})/N(\text{NH}) \sim 30\text{--}100$. It is interesting that the high NH abundance in diffuse clouds is a factor of ~ 40 higher than predicted by gas-phase chemical models (Meyer &

Roth 1991). The latter has been used by Wagenblast et al. (1993) and Crawford & Williams (1997) to **argue for** grain-surface production of NH. In principle, this process could also help to enhance the NH abundance in Arp 220, because the dust in the nuclei has been found to be warm so that grain mantles could efficiently evaporate, and also because in an environment with enhanced cosmic rays, as expected from a starburst and the consequent high rates of supernovae, **or an AGN**, the release of grain mantles to the gas phase by means of sputtering should be also enhanced. However, hydrogenation of NH should in principle continue until saturation, because indeed we observe NH_3 with a column density twice of NH. The issue that now arises is that, if hydrogenation generally completes, then a very low NH-to- NH_3 abundance ratio would be expected, and if it does not complete like in the models of Wagenblast et al. (1993), the scenario fails because of the low relative abundance found for NH_2 . In Sgr B2, for example, $\text{NH}:\text{NH}_2:\text{NH}_3=1:10:100$ (GRC04), and NH_2 is found to be fairly abundant (van Dishoeck et al. 1993).

One possible solution for the low NH_2 abundance is that the already invoked enhancement of cosmic rays deeply affects the ion-molecule gas-phase chemistry. Federman, Weber, & Lambert (1996) have shown that the high NH abundance found in some diffuse galactic environments could be explained through cosmic ray ionization of atomic nitrogen, followed by hydrogen abstraction reactions that form NH_n^+ and dissociative recombination that yields NH. The slight endothermicity of $\text{N}^+ + \text{H}_2 \rightarrow \text{NH}^+ + \text{H}$ (Millar, Farquhar, & Willacy 1997) is not a problem here, given the high dust temperatures in the nuclei. If in Arp 220 the cosmic-ray ionization of N is enhanced, the above scheme could give rise to high NH abundances. Furthermore, both NH_2 and NH_3 would be much less abundant if photodissociation is important in those regions. NH_3 would be formed primarily in grain mantles through nearly complete hydrogenation, thus again keeping the NH_2 abundance low, and released to the gas phase in widespread hot core regions relatively shielded from UV fields. H_2O could also follow this last process.

A chemistry deeply influenced by ion-neutral reactions have been also invoked by Aalto et al. (2002) to explain the high emission from HNC rel-

ative to HCN in Arp 220 and other luminous infrared galaxies. Furthermore, Aalto et al. (2002) also found strong subthermal CN emission, indicative of gas at moderate densities and irradiated by UV fields (Rodríguez-Franco, Martín-Pintado, & Fuente 1998). In the most simple scenario, the molecular content of Arp 220 may thus be interpreted in terms of hot cores submitted to strong UV and X-ray fields, where enhanced evaporation of grain mantles and ion-molecule chemistry induced by cosmic ray ionization are also deeply affecting the relative molecular abundances.

7. Summary

We have analyzed the ISO/LWS spectrum of Arp 220 using radiative transfer models applied to both the continuum and line emission. Our main results are:

1. The continuum emission from 25 to 1300 μm is well reproduced with a two-component model: (a) the nuclei, with effective size of $0''.4$ and dust temperature of 106 K, which accounts for essentially the whole flux at 25 μm and at millimeter and submillimeter wavelengths, and (b) an extended region (ER), whose effective size is $2''$ and which dominates the continuum emission from 60 to 250 μm .
2. The extinction toward the nuclei is very high ($A_V \sim 10^4$ mag); the dust in the ER is heated through absorption of radiation emanating from the nuclei.
3. The spectrum of Arp 220 shows molecular lines of OH, H₂O, CH, NH, and NH₃, as well as the atomic [O I] 63 μm line in absorption and the [C II] 158 μm line in emission. **The outermost regions of the nuclei, along with the ER, are traced by the lines observed in the far-infrared.**
4. The high excitation lines of OH and H₂O are pumped through absorption of photons emitted by dust. Column densities of $N(\text{OH}) = 2 - 6 \times 10^{17} \text{ cm}^{-2}$ and $N(\text{H}_2\text{O}) = 2 - 10 \times 10^{17} \text{ cm}^{-2}$ are derived toward the nuclei. In the ER, $N(\text{OH}) \sim 2 \times 10^{17} \text{ cm}^{-2}$ and $N(\text{H}_2\text{O}) \sim 3 \times 10^{16} \text{ cm}^{-2}$. We found it necessary to invoke a third component, or halo, to match the low-lying lines of OH and H₂O; this halo has column densities that are similar to those found toward the Galactic Center ($N(\text{OH}, \text{H}_2\text{O}) \sim 1.5 \times 10^{16} \text{ cm}^{-2}$).
5. The CH line detected in the far-infrared spec-

trum of Arp 220 is assumed to arise from the halo, and the inferred column density is $N(\text{CH}) \sim 2 \times 10^{15} \text{ cm}^{-2}$. This value is also similar to that found toward the Galactic Center.

6. Models for NH and NH₃ indicate high column densities toward the nuclei, $N(\text{NH}) \sim 1.5 \times 10^{16} \text{ cm}^{-2}$ and $N(\text{NH}_3) \sim 3 \times 10^{16} \text{ cm}^{-2}$. The upper limit found for the column density of NH₂ is much lower, $N(\text{NH}_2) \leq 2 \times 10^{15} \text{ cm}^{-2}$.

7. The [C II] 158 μm line strength is approximately reproduced by assuming that C⁺ is 100 times more abundant than OH. Our models predict that the line arises mainly from the ER, and that *non-PDR far-infrared emission, with possible extinction effects, is mostly responsible for the observed [C II] deficit in Arp 220.* The [O I] 63 μm line is also matched with an abundance of 250 relative to OH and absorption toward the nuclei, the ER, and the halo.

8. *PDR molecular chemistry plays a key role in the ER and contributes to the elevated OH abundance at the expense of H₂O. Toward the nuclei, however, important contributions from hot cores, and possibly from shocks, is most plausible. The nitrogen chemistry, and in particular the high NH abundance, seems to be strongly influenced by ion-neutral reactions triggered by cosmic ray ionization.*

We are grateful to J.R. Goicoechea for providing the ISO/LWS spectrum of Sgr B2 and for fruitful discussions. E. G-A thanks Spanish SEEU for funding support under project PR2003-0057, and the Harvard-Smithsonian Center for Astrophysics for its hospitality. This work has been partially supported by NASA Grant NAG5-10659, the NASA LTSA program and the Office of Naval Research.

REFERENCES

- Aalto, S., Polatidis, A.G., Hüttemeister, S., & Curran S.J. 2002, A&A, 381, 783
- Anantharamaiah, K.R., Viallefond, F., Mohan, N.R., Goss, W.M., & Zhao, J.H. 2000, ApJ, 537, 613
- Baluteau, J.-P. et al. 1997, A&A, 322, L33
- Carico, D.P., Keen, J., Soifer, B.T., & Neugebauer, G. 1992, PASP, 104, 1086

The far-infrared emission line and continuum spectrum of the Seyfert galaxy NGC 1068¹

Luigi Spinoglio

*Istituto di Fisica dello Spazio Interplanetario, CNR via Fosso del Cavaliere 100, I-00133
Roma, Italy*

luigi@ifsi.rm.cnr.it

Matthew A. Malkan

Physics & Astronomy Dept., UCLA, Los Angeles, CA 90095, USA

malkan@astro.ucla.edu

Howard A. Smith

Harvard-Smithsonian CfA, 60 Garden St., Cambridge, MA 02138, USA

hsmith@cfa.harvard.edu

Jacqueline Fischer

Naval Research Laboratory, Code 7213, Washington DC 20375, USA

Jackie.Fischer@nrl.navy.mil

ABSTRACT

The prototypical Seyfert type 2 galaxy NGC 1068 has been observed with the *Long Wavelength Spectrometer* (LWS) onboard the *Infrared Space Observatory* (ISO, ESA). This provides the first complete far-infrared spectrum from 43 to 197 μ m. In addition to the 7 expected ionic fine structure emission lines, we also detect OH rotational lines at 79, 119 and 163 μ m. Unlike any other galaxy yet observed, NGC 1068 shows all these lines in emission. To increase the information on the strong ionic emission lines powered either by the Seyfert nucleus and the starburst, we have included in our analysis measurements in the 2–35 μ m spectral range from the ISO *Short Wavelength Spectrometer* (SWS), as well as optical and ultraviolet lines from the literature. To model the observed line intensities we have considered three emission components: the AGN component, the starburst component originated from the circumnuclear ring at $\sim 15''$ from

the center and the nuclear starburst component. Following the guidelines of a recent work, the nuclear emission line spectrum from the AGN was modeled using two components photoionization models with constant densities of 2000 cm^{-3} and 10^4 cm^{-3} , respectively, and emission regions extending from a distance from the center of $\sim 20 \text{ pc}$ to $\sim 200 \text{ pc}$. We have adopted three different ionizing continua illuminating the AGN narrow line region: the first one has a large absorption dip around 4 Ryd ; the second has the standard broken power-law shape generally used for NGC1068 and the third has a big blue bump peaking at $\sim 10 \text{ Ryd}$. We find that the UV to mid-IR emission line spectrum originated from the AGN cannot be used to severely constrain the ionizing continuum that illuminates the NLR of NGC1068, contrary to previous results. While the presence of a *big blue bump* is ruled out, our modeled spectra do not require the presence of a large dip at 4 Ryd ., but are consistent also with the canonical power-law type ionizing spectrum.

We have used the Br γ emission from the circumnuclear ring and that one originated from the nuclear region to normalize the starburst emission of the second and third component, respectively. The ionizing continua for the starburst models have been derived from starburst synthesis models.

Three of the FIR lines of OH have been detected in NGC1068, and we present the first results of our modeling, which suggests the gas lies in small clouds, about 0.1 pc in size, with densities of $\leq 10^4 \text{ cm}^{-3}$ at the outer edges.

Subject headings: galaxies: individual (NGC 1068) – galaxies: active – galaxies: nuclei – galaxies: Seyfert – galaxies: emission lines – galaxies: starburst – infrared: galaxies.

1. INTRODUCTION

NGC 1068 is among the most studied active galaxies. It is known as the archetype Seyfert type 2 galaxy, it is nearby, with a measured redshift $z=0.0038$ (Huchra et al. 1999) (corresponding to a distance of $D=15.2 \text{ Mpc}$, adopting $H_0=75 \text{ km s}^{-1} \text{ Mpc}^{-1}$), providing a scale of only $\sim 74 \text{ pc}''$, bright ($L_{\text{IR}} = 2 \times 10^{11} L_{\odot}$ Bland-Hawthorn et al. 1997) and it has been extensively observed and studied in detail from X-rays to radio wavelengths. Around

¹ISO is an ESA project with instruments funded by ESA Member States (especially the PI countries: France, Germany, the Netherlands and the United Kingdom) and with the participation of ISAS and NASA.

the active nucleus, NGC 1068 has a central nuclear star cluster extending $\sim 0.6''$ (Thatte et al. 1997). Moreover, a stellar bar of 2.3kpc of size has been observed in the near-IR (Scoville et al. 1988; Thronson et al. 1989), which is surrounded by a circumnuclear starburst ring. Mapping revealed that the infrared emission in NGC 1068 was due to both the Seyfert nucleus (dominating the $10\mu\text{m}$ emission) and to the star forming regions in the bright circumnuclear ring of $\sim 3\text{kpc}$ in diameter (emitting most of the luminosity at $\lambda > 30\mu\text{m}$) (Telesco et al. 1984). A $Br\gamma$ imaging study (Davies, Sugai & Ward 1998) reveals a similar morphology. It indicates that a short burst of star formation occurred throughout the circumnuclear ring ($15\text{-}16''$ in radius) perhaps within the last 4-40 Myr. CO interferometer observations revealed molecular gas very close to the nucleus ($\sim 0.2''$) suggesting the presence of $\sim 10^8 M_\odot$ within the central 25pc (Schinnerer et al. 2000). Recent high resolution H_2 line emission mapping indicates the presence of two main emission knots with a velocity difference of 140 km/s, that, interpreted as quasi-keplerian velocity, would imply a central enclosed mass of $10^8 M_\odot$ (Alloin et al. 2001).

In this article, we present the first complete far-infrared spectrum from 43 to $197\mu\text{m}$ showing both atomic and molecular emission lines (§2.). We model the far-IR continuum emission using gray body functions (§3.), we also model the composite UV- to far-IR atomic emission line spectrum, as derived by combining literature observations with our data, using photoionization models of both the active nucleus (§4.1) and the starburst components (§4.2-4.3). Moreover, montecarlo radiation transfer models have been used to account for the detected far-IR molecular lines (§5.). Our conclusions are then given in §6.

2. OBSERVATIONS

NGC 1068 was observed with the Long Wavelength Spectrometer (LWS) (Clegg et al. 1996) on board the Infrared Space Observatory (ISO) (Kessler et al. 1996), as part of the Guaranteed Time Programme of the LWS instrument team. The full low resolution spectrum ($43\text{-}197\mu\text{m}$) of NGC 1068 was collected during orbit 605 (July 13, 1997). Two on-source full scans (15,730 seconds of total integration time) and two off-source ($6' \text{ N}$) scans of the [CII] $158\mu\text{m}$ line (3,390 seconds of total integration time) were obtained. On- and off-source scans had the same integration time per spectral step. Because of the design of the LWS spectrometer, simultaneously with the $158\mu\text{m}$ data, a short spectral scan of equal sensitivity to the on-source spectrum was obtained at sparsely spaced wavelengths across the LWS range.

The LWS beam is roughly independent of wavelength and equal to about 80 arcsec. The spectra were calibrated using Uranus, resulting in an absolute accuracy better than

30% (Swinyard et al. 1996). The data analysis has been done with ISAP², starting from the auto-analysis results processed through the LWS Version 7-8 pipeline (July 1998). To be confident that newer versions of the pipeline and calibration files did not yield different results, we have compared our data with the results obtained using pipeline 10.1 (November 2001) and we did not find significant differences on both the line fluxes and the continuum. To increase the signal-to-noise ratio, all the full grating scans taken on the on-source position have been coadded, as well as the two sets of data on the off-source position. No signal was detected in the off-source position. The emission line fluxes were measured with ISAP, which fits Gaussians on top of a local continuum. In every case the observed line width was consistent with the instrumental resolution of the grating, which is typically 1000 km/sec. The integrated line fluxes measured independently from data taken in the two scan directions agreed very well, to within 10%. LWS has a known tendency for fringing to produce spurious ripples in the continuum baseline (Swinyard et al. 1998). Fortunately, these fringing ripples are hardly noticeable in our LWS spectrum, presumably because the far-IR continuum is centrally concentrated towards the center of the LWS 80 arcsec beam.

Besides the LWS observations, we also use the SWS observations presented by Lutz et al. (2000), to extend the wavelength and ionization-level coverage. Table 1 presents all the ISO line flux measurements, including those from the SWS.

3. THERMAL CONTINUUM SPECTRUM

The 50-200 μ m far-infrared spectral energy distribution (SED) of NGC1068 can be fitted by the combination of different gray body functions. Fig. 1 shows the observed LWS spectrum of NGC1068, together with a fit with the main gray body component at T=32K, a warmer component at T=65K and a cooler one at T=20K. The dust emissivity has been assumed to be proportional to the inverse square of the wavelength (i.e., the flux density is $S_\lambda = B_\lambda(T) \times \lambda^{-\beta}$ with $B_\lambda(T)$ the Planck function at the wavelength λ and temperature T and $\beta=2$). We have adopted this steep dust emissivity law because it fits better than flatter laws the 12-200 μ m SED of Seyfert and starburst galaxies, as shown in Spinoglio, Andreani & Malkan (2002).

²The ISO Spectral Analysis Package (ISAP) is a joint development by the LWS and SWS Instrument Teams and Data Centers. Contributing institutes are Centre d'Etude Spatiale des Rayonnements (France), Institute d'Astrophysique Spatiale (France), Infrared Processing and Analysis Center (United States), Max-Planck-Institut für Extraterrestrische Physik (Germany), Rutherford Appleton Laboratories United Kingdom) and the Space Research Organization, Netherlands.

Because of the large (3) number of components used, we do not claim that the proposed fit is unique, however it fits the 50-200 μ m spectrum fairly well (reduced $\chi^2=0.40$, corresponding to a probability of $P>98\%$) and it is derived from a physically consistent view of the various dust thermal components in Seyfert galaxies (see e.g. Spinoglio, Andreani & Malkan 2002).

4. THE FINE STRUCTURE LINES

To be able to better constrain the modeling of the line emission of NGC1068, we have combined our far-infrared fine structure line measurements (Table 1) with ultraviolet, optical and infrared spectroscopic data from the literature (Kriss et al. 1992; Marconi et al. 1996; Thompson 1996; Lutz et al. 2000). The complete emission line spectrum of NGC1068 from the ultraviolet to the far-IR includes several low-ionization lines that are primarily produced outside the narrow line region (NLR) of the active nucleus, as well as intermediate ionization lines that originate from both starburst and AGN emission. For this reason, we find that no single model satisfactorily explains all the observed emission lines. We identify three components:

- an AGN component (the NLR), exciting the high ionization lines and contributing little to the low-to-intermediate ionization lines;
- a starburst component in the circumnuclear ring of the galaxy (e.g. Davies, Sugai & Ward 1998) that produces part of the emission of the intermediate ionization lines;
- another starburst component that originates from the nucleus of NGC1068.

We will also see that a photo-dissociation region (PDR) (e.g. Kaufman et al. 1999), in the interstellar medium of the galaxy, has also to be added to fully model the low ionization and neutral forbidden lines.

The contributions of the starburst and PDR emission can be estimated from the CII/OI/OIII line ratio diagram, as used by Malkan et al. (2002). However, for this galaxy we can obtain a more direct measurement of the starburst/HII region components, using the high spatial resolution available from ground-based near-IR Fabry-Perot imaging and grating spectroscopy. As shown in §4.2 and §4.3, we have taken the Br_γ fluxes originated in the ring-like star forming complex and from the nuclear region of NGC1068, respectively from Davies, Sugai & Ward (1998) and from Oliva & Moorwood (1990).

In the following of this section, we will examine separately the three components that are producing the composite fine structure emission line spectrum of NGC1068, for which we propose three different computations in §4.4. We will leave for §4.5 the estimate of the model parameters of the PDR emission produced from the ISM of the galaxy.

4.1. Modeling the AGN

The first predictions based on photoionization models of the mid to far-infrared spectrum originated from the Narrow Line Regions (NLR) of active galaxies have been done by Spinoglio & Malkan (1992), well before the observations could be collected. The specific photoionization modeling of only the high ionization emission lines unambiguously produced by the Seyfert nucleus of NGC1068 has been done previously by Alexander et al. (2000). Following their results, we have simulated their models, although using a different photoionization code, CLOUDY (Version 94.00 Ferland 2000), and then we have varied the shape of the ionizing continuum. As already mentioned in the previous section, our goal was not only to test if the Alexander et al. (2000)'s results were unique, but also to add together all different photoionized components originated from different emission regions to model the complete emission line spectrum of NGC1068. We have assumed two component models for the AGN, with the same parameters as in Alexander et al. (2000): the first component has a constant Hydrogen density of 10^4cm^{-3} , an ionization parameter $U=0.1$, extends from ~ 20 to ~ 80 pc from the center, it has a covering factor $c=0.45$ and a filling factor of 10^{-4} with a radial dependence of the form r^{-2} ; the second component has a density of $2 \times 10^3 \text{cm}^{-3}$, an ionization parameter $U=0.01$, extends from ~ 140 to ~ 190 pc from the center, it has a covering factor $c=0.29$ and a filling factor of 10^{-3} without any radial dependence. We have assumed also the "low Oxygen" abundances adopted by Alexander et al. (2000), to be able to compare in the easiest way our results with theirs. Tables 2 and 3 report the results of the three AGN models we have chosen to fit the NGC1068 spectrum, together with the observed line fluxes: the line fluxes are given for each of the two components A and B, which are treated as independent, and the total flux for each model is simply the sum of the fluxes of the two components. The intrinsic nuclear spectrum of NGC 1068 has been inferred by Pier et al. (1994), we have modified this in the 1–100 Ryd region to model both the through derived by Alexander et al. (2000) and a *big blue bump*, as expected by the thermal emission of an accretion disk around the central black hole. Specifically, model A assumes the same ionizing spectrum that was derived from the best fit model of Alexander et al. (2000), i.e. with a deep through at 4 Rydberg ($\log f = -27.4, -29.0, -27.4, -28.2$ at 2, 4, 8 and 16 Ryd, respectively). Model B assumes the original ionizing spectrum derived from Pier et al. (1994). Model C assumes a Big Blue Bump spectrum on the top of the

Pier et al. (1994) ionizing continuum ($\log f = -25.8, -25.8, -25.8, -27.4$ at 2, 4, 8 and 16 Ryd, respectively). The three AGN ionizing continua are plotted in Fig.2. The inner and outer radii of the emission regions of the two components, 20, 80, 140 and 190pc, correspond to angular distances of about 0.27, 1.1, 1.9 and 2.6 ", respectively.

We can see from Tables 2 and 3 that only the AGN A and AGN B models, and not the AGN C model, represent fairly well most of the observed line fluxes, except for the low and intermediate ionization lines, that — as we expected — are also, and sometimes mainly, produced by starburst and PDR excitation (see Section 4.4). This first result rules out the presence of a big blue bump in the ionizing continuum of NGC1068. To be able to compare the modeled ultraviolet and optical lines with the observations, we also listed in Table 2 and 3 their dereddened fluxes, assuming two values for the extinction: $E_{B-V} = 0.4$ mag (Malkan & Oke 1983) and $E_{B-V} = 0.2$ mag (Marconi et al. 1996).

4.2. Modeling the starburst ring

NGC1068 is known to emit strong starburst emission from both its nucleus and the ring-like structure at 15-16 "from the nucleus, traced e.g. by the Br γ emission (Davies, Sugai & Ward 1998). To model this second component, we have considered how much of the Br γ line was emitted inside the different apertures of the ISO spectroscopic observations. In the smallest ISO-SWS aperture used (14 " \times 20 ") no Br γ emission is detected from the ring. In the next aperture (14 " \times 27 ") Davies, Sugai & Ward (1998)'s regions I, J, K and L are included, for a total Br γ intensity of $\sim 10^{-14}$ erg s $^{-1}$ cm $^{-2}$. The largest SWS aperture (20 " \times 33 "), in addition to the above regions, also contains regions H, E, D and C, for a total Br γ intensity of $\sim 2.2 \times 10^{-14}$ erg s $^{-1}$ cm $^{-2}$. Finally, in the large LWS aperture (~ 80 " 2), all the ring-like Br γ emission is contained, $\sim 5.9 \times 10^{-14}$ erg s $^{-1}$ cm $^{-2}$.

Assuming that applies "case B" recombination, we can scale the Br γ intensity into H α intensity (from Table 4.4 of Osterbrock 1989):

$$j_{Br\gamma}/j_{H\alpha} = j_{Br\gamma}/j_{H\alpha} \cdot j_{Br\gamma}/j_{H\epsilon} \cdot j_{H\epsilon}/j_{H\beta} \cdot j_{H\beta}/j_{H\alpha} = 0.0097$$

For the three increasing apertures (14 " \times 27 ", 20 " \times 33 " and 80" 2 respectively) we have derived an H α intensity from the starburst ring of 10^{-12} , 2.3×10^{-12} and 6.1×10^{-12} erg s $^{-1}$ cm $^{-2}$, respectively. We have used these values to derive the modeled line intensities from the CLOUDY code, that was used adopting H α as normalizing line.

We have chosen three starburst synthesis models Starburst99 from Leitherer et al.

(1999), as input ionizing spectra for the CLOUDY photoionization code. These ionizing continua are shown in Fig. 3. For the models with instantaneous star formation law, we adopted a total mass of $M = 10^6 M_{\odot}$, and a duration of 5 Myr, while for the models with continuous star formation law, we have chosen a star formation rate of $1 M_{\odot} \text{ yr}^{-1}$. For both types of models we adopted a Salpeter IMF ($\alpha=2.35$), a lower cut-off mass of $1 M_{\odot}$, an upper cut-off mass of $100 M_{\odot}$, abundances of $Z=0.008$ and nebular emission included.

We report in Table 4 the line fluxes predicted using CLOUDY for the two instantaneous models (SBR A and B, where SBR stands for Starburst Ring) and the four continuous models (SBR C, D, E and F). The adopted parameters for the photoionization models are given in the table.

4.3. Modeling the nuclear starburst

We have computed also the expected emission that originates from the nuclear starburst present in NGC1068. To model this third component, we have used the Br γ intensity of $13 \times 10^{-14} \text{ erg s}^{-1} \text{ cm}^{-2}$, which was observed in a $6'' \times 6''$ aperture (Oliva & Moorwood 1990). As a first order approximation, we made the assumption that half of the Br γ intensity observed in the nuclear region is originated from the nuclear starburst, while the other half is produced in the NLR. Then we used the two models F and E, described in the previous section. The predicted line fluxes are listed in Table 3, together with the model parameters.

4.4. Adding the three components

Summing up the line intensities of each one of the three components, the composite spectrum of NGC1068 can be derived and compared with the observed one. We have chosen three combinations to compute the composite models, each one with a different AGN model: 1) the first one (that we name CM1, as Composite Model 1) with the AGN ionizing continuum as suggested by Alexander et al. (2000) (model AGN A), a low-ionization nuclear starburst (model SBN F) and an high-ionization starburst ring (model SBR E); 2) the second (CM2) with the original Pier et al. (1994) (model AGN B), the same nuclear starburst and starburst ring models as for CM1; 3) the third (CM3) with the hypothetical bump (model AGN C), and again the same starburst models. The results of these three composite models are given in Table 5, compared to the observed and dereddened values, assuming the two choices for the extinction (see §4.1). We also show the results of the three composite models in a graphical way in Fig. 4 and Fig. 5, where the modeled to the observed flux ratio is given

for each line and for the two values assumed of the extinction, respectively.

Taking the higher value for the optical extinction (Fig.5), most of the lines (33/43) of the first model (CM1) and almost all the lines (37/43) of the second composite model (CM2) are predicted within a factor 3 from the observed/dereddened values. The third composite model (CM3) is much less successful, having 14 lines badly under- or over-predicted. Considered the fact that our composite models are made of three different physical components, aimed to reproduce more than forty emission lines, the agreement between the first two composite models and the data is satisfactory and, as already noted, excludes the possibility that a big blue bump is present in the ionizing spectrum of NGC1068. On the other hand we cannot confirm the presence of the dip suggested by Alexander et al. (2000).

4.5. Modeling the PDR

An accurate model for the PDR emission originating in the ISM of the NGC1068 galaxy is beyond the scope of the present article, however it is possible to check what are the main parameters of the PDR, i.e. far-ultraviolet field (G_0) and Hydrogen density (n). To do this, we just subtract off the modeled intensities of the three components from the observed fluxes of [OI]63 μ m, [OI]145 μ m and [CII]158 μ m, then we take the ratios of these lines, namely [OI]63 μ m/[CII]158 μ m and [OI]63 μ m/145 μ m and compare them with the Kaufman et al. (1999) PDR models. Following this simple procedure, we find that for the first composite model $\log G_0 = 2$ and $\log n = 3.3$, while for the other two composite models $\log G_0 = 3$ and $\log n = 2.5$.

5. THE OH LINES

In NGC 1068, we detect three of the OH rotational lines. Two of the lines are to the ground state $^2\Pi_{3/2}3/2$ level: the in-ladder 119 μ m fundamental line from the $^2\Pi_{3/2}5/2$ level, and the cross ladder 79 μ m line from the lowest, $^2\Pi_{1/2}1/2$ level. The third line is the lowest transition of the $^2\Pi_{1/2}$ ladder: the 163 μ m line between the $J=1/2$ and $J=3/2$ levels. These three lines are all seen in emission in NGC 1068, in striking contrast with the OH emission we have measured from other bright infrared galaxies such as Arp 220 (Fischer et al. 1999), Mrk 231 (Harvey et al. 1999), NGC 253 (Bradford et al. 1999), M 82 (Colbert et al. 1999), in which the 119 micron fundamental is in absorption (the 79 μ m line is seen both in emission and absorption; the 163 μ m line is always seen in emission). In addition to these three detections, our ISO LWS observations were able to obtain useful limits on

four of the other eleven FIR OH lines in the LWS band that arise between the lowest eight rotational levels. The lines are indicated in the overall LWS spectrum of NGC1068 in Fig. 1, are shown in detail in Fig. 6 and tabulated in Table 1, while a comparison between observed and modeled fluxes is given in Table 6.

We used a montecarlo radiative transfer code to model the lines in NGC 1068, as part of a detailed study of all the OH lines observed by ISO in galaxies (Smith 2002; Smith et al. 2003). The code was developed by the Submillimeter Wave Astronomy Satellite (SWAS) mission (Ashby et al., private com.), and is a modification of the original Bernes code, but includes a treatment of continuum photons from dust mixed in with the gas – a particularly essential feature for OH, which is pumped in many cases by absorption of $35\ \mu\text{m}$ continuum. In addition the code corrects for some previous errors encountered at large optical depths, also an issue of importance for OH which has a very strong matrix element (1.67 Debye), and a fundamental line transition rate of about $0.1\ \text{s}^{-1}$ – about 1000 times greater than CO rates. The code also includes an ability to handle a wide range of molecules besides rigid rotors.

The montecarlo code is one-dimensional; so far this constraint does not seem to preclude a reasonable physical explanation. The code takes in input a series of concentric shells, each of which is specified as to size, gas and dust temperature, H_2 density, velocity and turbulent velocity width, and molecular abundance relative to H_2 . The model allows the wavelength dependence of the dust emissivity to be independently set. The SWAS version of the montecarlo code calculates the populations of the molecular levels in each shell, and the output of this calculation, iterated until it converges, is then fed into a radiative transfer code that calculates the line profiles as seen by an external observer looking at the cloud.

The montecarlo output by itself is not constrained to be self-consistent; for example, the input parameters need not conserve luminosity between shells. To obtain this self-consistency, which we determined was essential for a satisfactory model of the continuum flux, we used the DUSTY code (Ivezic & Elitzur 1997) to model the continuum and generate a set of shell parameters that provided this consistency. We then iterated the DUSTY model with the montecarlo line outputs. Although we do not claim this technique gives a unique solution for the cloud structure, it does give a canonical model consistent with the observations.

We take as a starting assumption that the clouds of gas and dust producing the OH emission are heated from the inside, rather than dominated by external heating; the most successful models implied the cooler volumes were substantially larger than the hotter volumes. To produce consistent emission, especially in the $119\ \mu\text{m}$ fundamental line, we find that the clouds are small and dense. The best fit agreement has clouds of dimensions of

~ 0.2 pc in radius, and densities of $\leq 10^4 \text{cm}^{-3}$ at the outer edges, increasing towards the center with a power law behavior of $(R/R_0)^{1.25}$. The temperature in the outer shells is about 22K, increasing inwards approximately with a power law dependence $(R/R_0)^{0.68}$. Our best fit model has a total column density of H_2 in each cloud is $1.5 \times 10^{24} \text{cm}^{-2}$, and a relative abundance of OH in the model is 10^{-7} ; note that we take OH to be absent in the hot, inner portions of the cloud ($T > 300\text{K}$). The strong lines of OH are therefore very optically thick, and precise radiative transfer calculations like the present modeling are essential.

As can be seen from Table 6, the montecarlo code predicts the line flux ratios to the $119\mu\text{m}$ feature to within a factor of 40% of the observed values. The limits to the observed fluxes in all the weaker lines are also consistent with this modeling. At a distance of 15.2 Mpc, the total number of clouds needed to produce the observed absolute flux in the lines and the continuum is $\sim 3 \times 10^7$. As for the continuum, the montecarlo code also successfully reproduces the continuum emission seen from NGC 1068, to within a factor of 2-3 in absolute flux density across the entire LWS spectrum, under the simple assumption that the dust is 1% of the gas by mass, and that it has the same temperature as the gas everywhere in the cloud. Although these constraints are not required by the code, they provide a good fit and are adequate for our general purposes here. The total mass in such an ensemble of clouds is approximately $9 \times 10^9 M_\odot$. This amount of mass is considerably larger than the value of $\sim 10^8 M_\odot$ estimated from CO interferometry in the core, but includes all of the galaxy in the ISO LWS beam of about $80''$, a much larger region than the circumnuclear CO observations. Papadopoulos & Seaquist (1999a) find that the mass in $1'$ might be $\sim 6 \times 10^9 M_\odot$, or perhaps even twice that - so, in good agreement with our values. Our modeling of the large beam ISO flux averages is unable to discriminate between nuclear clouds and non-nuclear clouds. Moreover, Papadopoulos & Seaquist (1999b) also find a gas/dust ratio up to 300 in the central $40''$, much more than the standard value of 100 that was adopted here.

The montecarlo code automatically calculates the velocity profile of each of the OH lines. We found that for a wide range of parameters the lines had both emission and absorption components, the result of cold gas in the line-of-sight to the warm center absorbing, while the cooler, outer shells emitted. Our observations of the $119\mu\text{m}$, feature in the galaxy NGC 253 (Bradford et al. 1999), for which we have ISO-LWS Fabry-Perot velocity resolved measurements, reveal this dual character. The detection we report here, of significant emission in NGC 1068, does not preclude the possibility that the actual line emission is substantially larger, but has been offset by some absorption at the line center by other components. Furthermore the model also suggests that the absorptions we typically detect at low LWS spectral resolution in other ISO galaxies may in fact show, at higher resolutions, a combination of emission plus absorption features.

By way of a self-consistent check, we have also used the montecarlo code to model, independently, the emission and absorption from this series of clouds in the two neutral oxygen [OI] lines at $63\mu\text{m}$ and $145\mu\text{m}$. The results are satisfactorily consistent with the observations. The [OI] $63\mu\text{m}$ and $145\mu\text{m}$ lines from these warm compact clouds are, respectively, estimated at $1.2 \times 10^{-12} \text{ erg s}^{-1} \text{ cm}^{-2}$ and $2.6 \times 10^{-14} \text{ erg s}^{-1} \text{ cm}^{-2}$, which correspond to only a few percent of the total observed emission (see Table 1). Obviously since the [OI] lines have their major contributions coming from other kinds of regions - photoionization, PDRs and shocks in particular - the significant conclusions to be drawn here are that the model for the OH lines is consistent with all the other observations.

Our conclusion is that NGC 1068 has a large component of relatively small, dense clouds of molecular gas and dust, heated internally. We cannot say from these data where these clouds are located in the large ISO beam, or what if any relationship they may have with the nuclear regions except that they do not appear to require either pumping or radiative effects from the nuclear region or its torus. A further analysis of the OH lines, in the context of other galaxies measured by ISO, is in preparation (Smith et al, 2003).

6. CONCLUSIONS

The main results of this article can be summarized as follows:

- The complete far-infrared (50-200 μm) spectrum of NGC1068 has been observed for the first time.
- The 50-200 μm continuum can be interpreted as thermal dust emission mainly due to three components at temperatures of 20, 32 and 65K, assuming a steep ($\beta=2$) dust emissivity law.
- The far-infrared ISO-LWS spectrum has been complemented with the mid-infrared data of ISO-SWS and with shorter wavelength (UV, optical and near-IR) literature data to assemble a composite atomic spectrum as complete as possible with the aim of modeling the different line emission components at work. This approach has been necessary especially because of the poor spatial resolution of the past space infrared spectrometers, which were not able to spatially separate the emission components. The lines have been interpreted as arising from three physically distinct components: the AGN component and two starburst components, the first one nuclear and the second one located in the ring at a radius of 15-16 " from the nucleus. Three composite models have been computed that vary mainly for their AGN component: the first one

has the ionizing continuum as derived from Alexander et al. (2000), showing a deep trough at energies of a few Rydberg; the second has the monotonically decreasing ionizing continuum given by Pier et al. (1994) and the third has a big blue bump. Two values of the visual extinction ($E_{B-V} = 0.2$ and 0.4) have been adopted to correct the optical and ultraviolet line fluxes. If we assume the higher value for the reddening, the agreement between the two composite models that do not show the presence of a big blue bump and the observed emission line spectrum is rather satisfactory, taking into account either the simplicity of the photoionization models chosen to avoid dealing with too many free parameters and the large number of lines which are originated in different physical regimes.

- The radiative transfer modeling of the three lines of OH detected in NGC1068 suggests that the emission can be originated in small gas clouds, about 0.1pc in size, with densities of $\leq 10^4 \text{cm}^{-3}$ at the outer edges.

The authors acknowledge the LWS Consortium, lead by Prof. Peter Clegg, for having built and operated the LWS instrument and solved many instrumental and data reduction problems. The ESA staff at VILSPA (Villafranca, Spain) is also acknowledged for the ISO mission operations.

REFERENCES

- Alexander, T., Lutz, D., Sturm, E., Genzel, R. et al. 2000, ApJ, 536, 710.
- Alloin, D. et al. 2001, A&A, 369, L33.
- Bland-Hawthorn, J., et al., 1997, ApSS, 248, 9.
- Bradford, C.M., et al., 1999, Proc.of the Conference "The Universe as seen by ISO", Paris, France, 20-23 October 1998 (ESA SP-427),p.861.
- Clegg, P.E., et al. 1996, A&A, 315, L28.
- Colbert, J., et al., 1999, ApJ, 511, 721.
- Davies, R.I., Sugai,H., and Ward, M.J., 1998, MNRAS, 300, 388
- Ferland, G.J., 2000, RevMexAA,(Serie de Conferencias), Vol.9, 153

- Fischer, J., et al. 1999, Proc.of the Conference "The Universe as seen by ISO", Paris, France, 20-23 October 1998 (ESA SP-427),p.817.
- Harvey, V.I., et al., 1999, Proc.of the Conference "The Universe as seen by ISO", Paris, France, 20-23 October 1998 (ESA SP-427),p.889.
- Huchra, J.P., Vogeley, M.S. & Geller, M.J. 1999, ApJS, 121, 287.
- Kaufman, M.J., Wolfire, M.G., Hollenbach, D.J., Luhman, M.L. 1999, ApJ, 527, 795.
- Kessler, M.F. et al.,1996, A&A, 315, L27
- Kriss, G.A. et al. 1992, ApJ, 394, L37
- Ivezic, Z., & Elitzur, M. 1997, MNRAS, 287, 799
- Leitherer, C., and Heckman, T.M., 1995, ApJSS, 96, 9.
- Leitherer, C., et al. 1999, ApJS, 125, 489.
- Lutz, D. et al., 2000, ApJ, 536, 697.
- Marconi, A., et al. 1996, A&A, 315, 335.
- Malkan, M. A., et al. 2002, in prep.
- Malkan, M. A. & Oke, J. B. 1983, ApJ, 265, 92.
- Oliva, E. & Moorwood, A.F.M. 1990, ApJ, 348, L5.
- Osterbrock, D.E. 1989, Astrophysics of gaseous nebulae and active galactic nuclei, University Science Books, Mill Valley, California, p.84.
- Papadopoulos,P.P. & Seaquist, E.R. 1999, ApJ, 514,L95.
- Papadopoulos,P.P. & Seaquist, E.R. 1999, ApJ, 516,114.
- Pier, E.A., et al. 1994, ApJ, 428, 124.
- Schinnerer, E., et al. 2000, ApJ, 533, 850.
- Smith, H.A., 2002, Proceedings of the the Second Maryland Conference on FIR Astronomy.
- Smith, H. A., et al., 2003, in prep.
- Spinoglio, L., Andreani, P. & Malkan, M.A., 2002, ApJ, 572, 105.

Spinoglio, L. & Malkan, M.A., 1992, ApJ, 399, 504.

Scoville, N.Z., Matthews, K., Carico, D.P., Sanders, D.B. 1988, ApJ, 327, L61.

Swinyard, B.M., et al. 1996, A&A, 315, L43.

Swinyard, B.M., et al. 1998, Proc. SPIE, A.M. Fowler (Ed.), Vol.3354, P.888.

Telesco, C.M., et al., 1984, ApJ, 282, 427.

Thatte, N., et al. 1997, ApJ, 490, 238.

Thompson, R.I., 1996, ApJ, 459, L61.

Thronson, H.A. et al. 1989, ApJ, 343, 158.

This preprint was prepared with the AAS L^AT_EX macros v5.0.

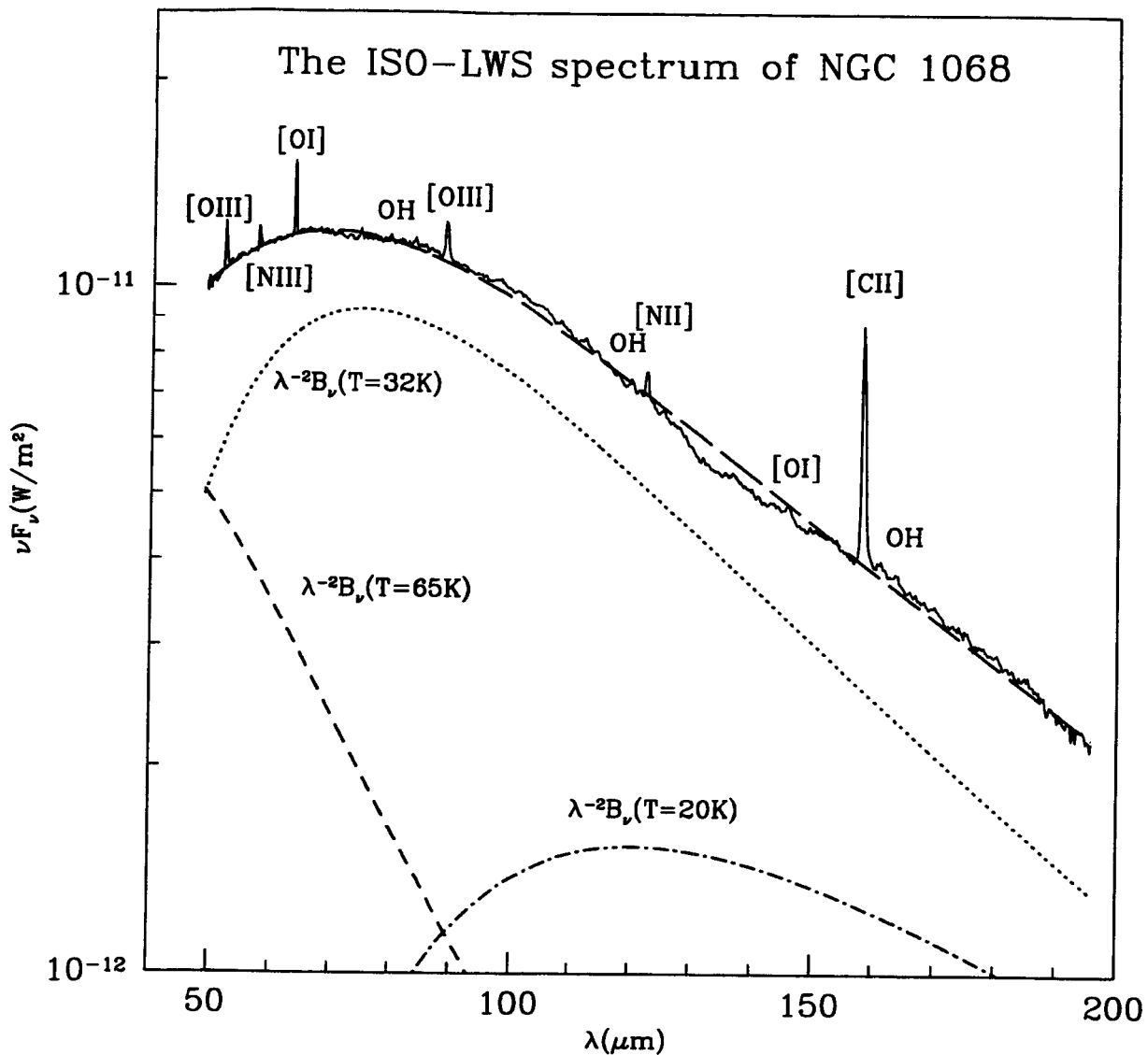


Fig. 1.— The ISO-LWS spectrum of NGC1068. The long-dashed line, which is fitting the data (reduced $\chi^2=0.40$, corresponding to a probability of $P>98\%$) represents the sum of the three different grey-body functions: dotted line: main component at $T=32\text{K}$; dotted-dashed line: cold component at $T=20\text{K}$; short-dashed line: warm component at $T=65\text{K}$.

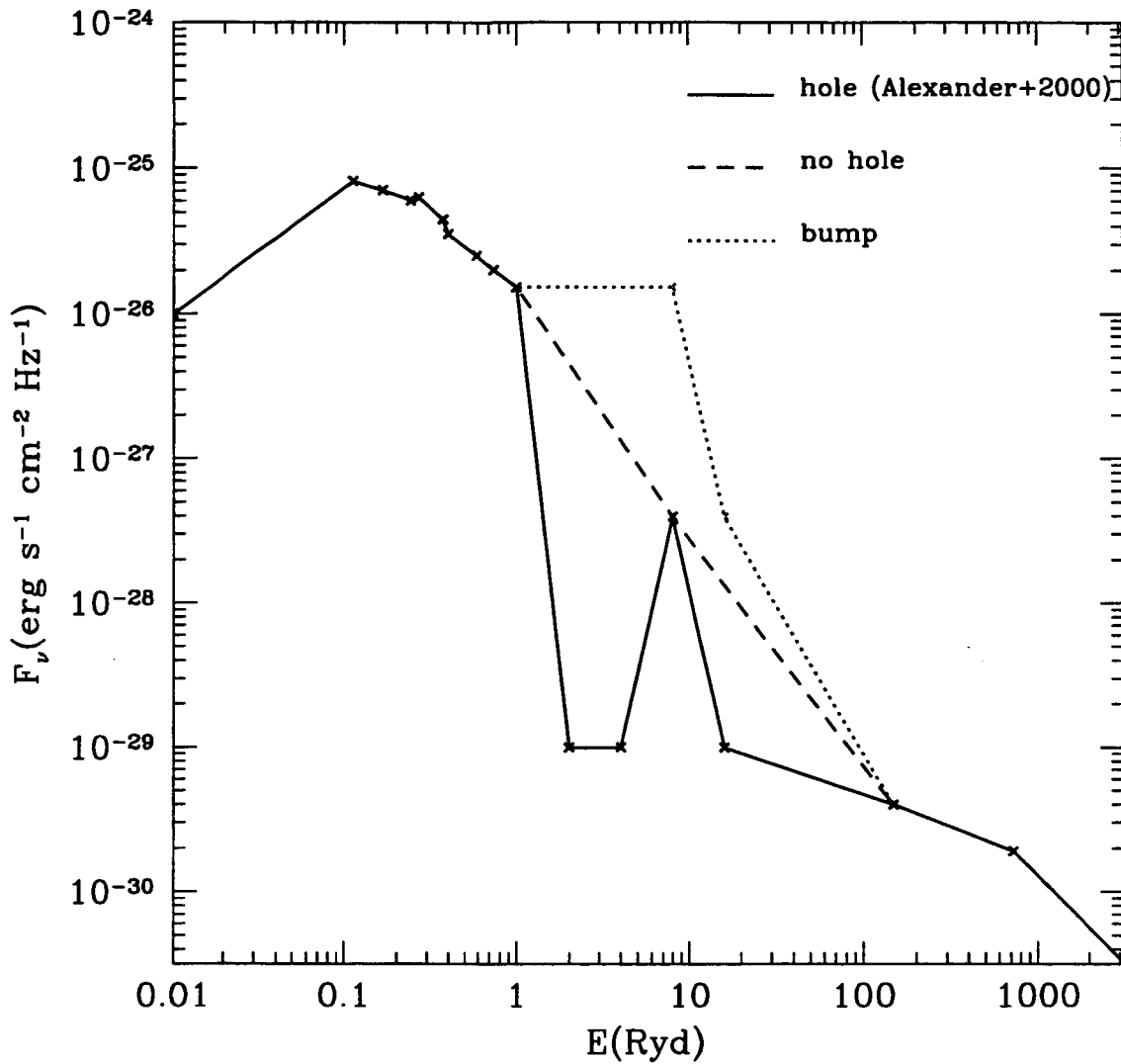


Fig. 2.— The AGN ionizing continua used as input for the photoionization models of NGC1068. The three continua differ in the frequency region between $1 > E_{Ryd} > 100$, while outside this region the Pier et al. (1994) spectrum was adopted. The solid line shows the continuum derived from Alexander et al. (2000); the dashed line shows a simple power law interpolation; the dotted line shows the presence of the predicted "big blue bump".

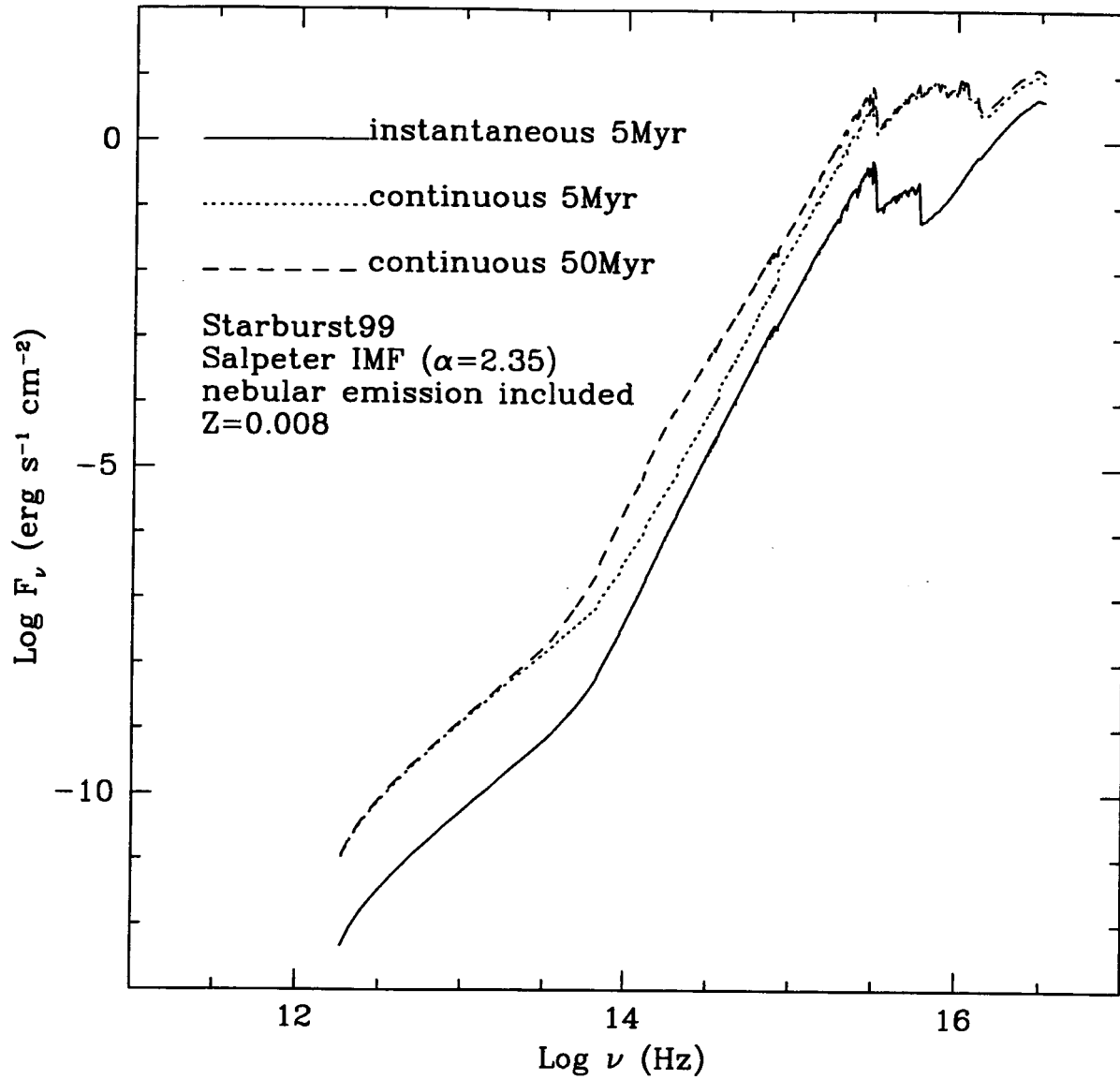


Fig. 3.— The starburst ring ionizing continua used as input for the photoionization models of NGC1068. The three continua are taken from Leitherer et al. (1999).

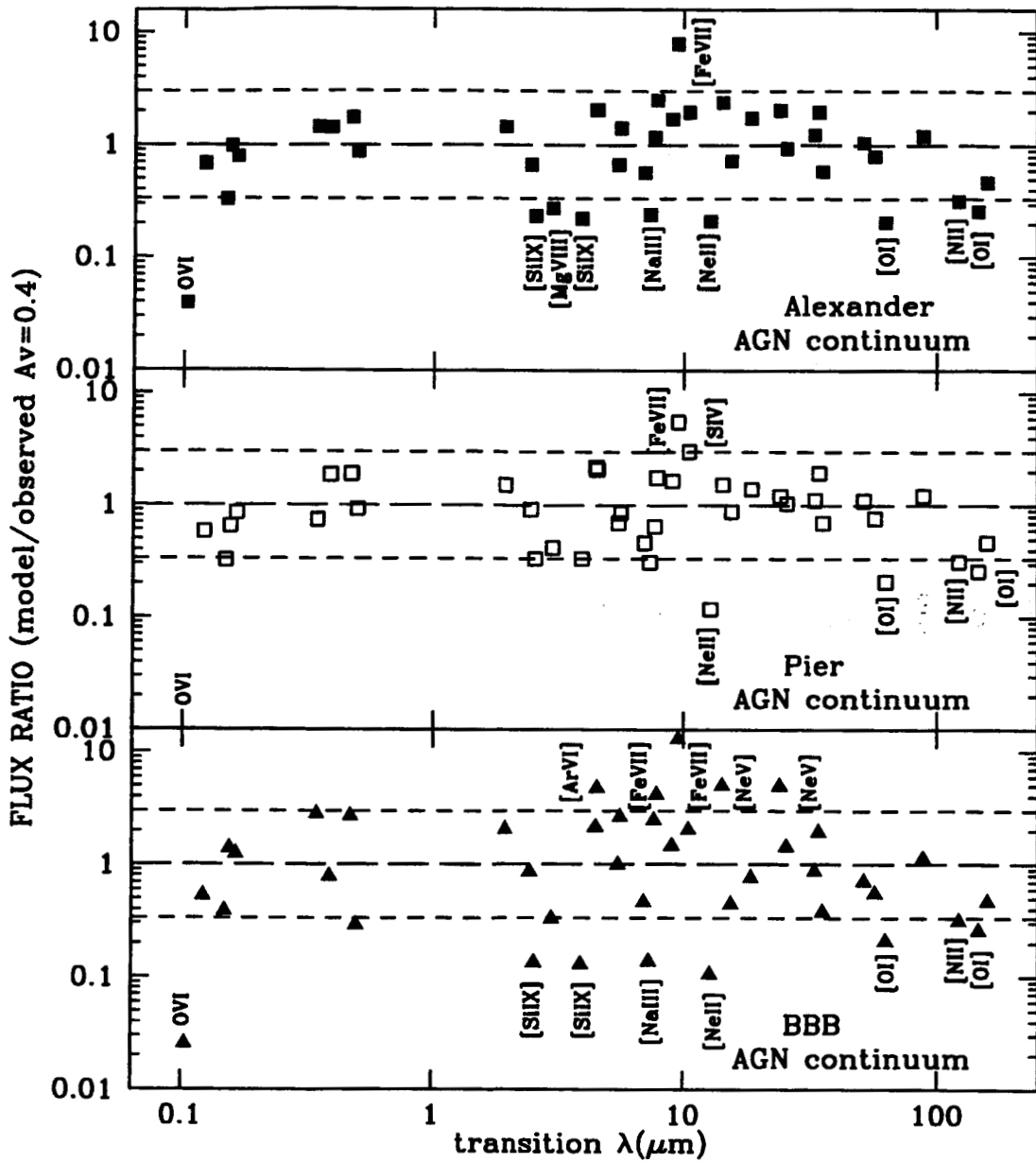


Fig. 5.— Same as the previous figure, but with $E(B-V)=0.4$.

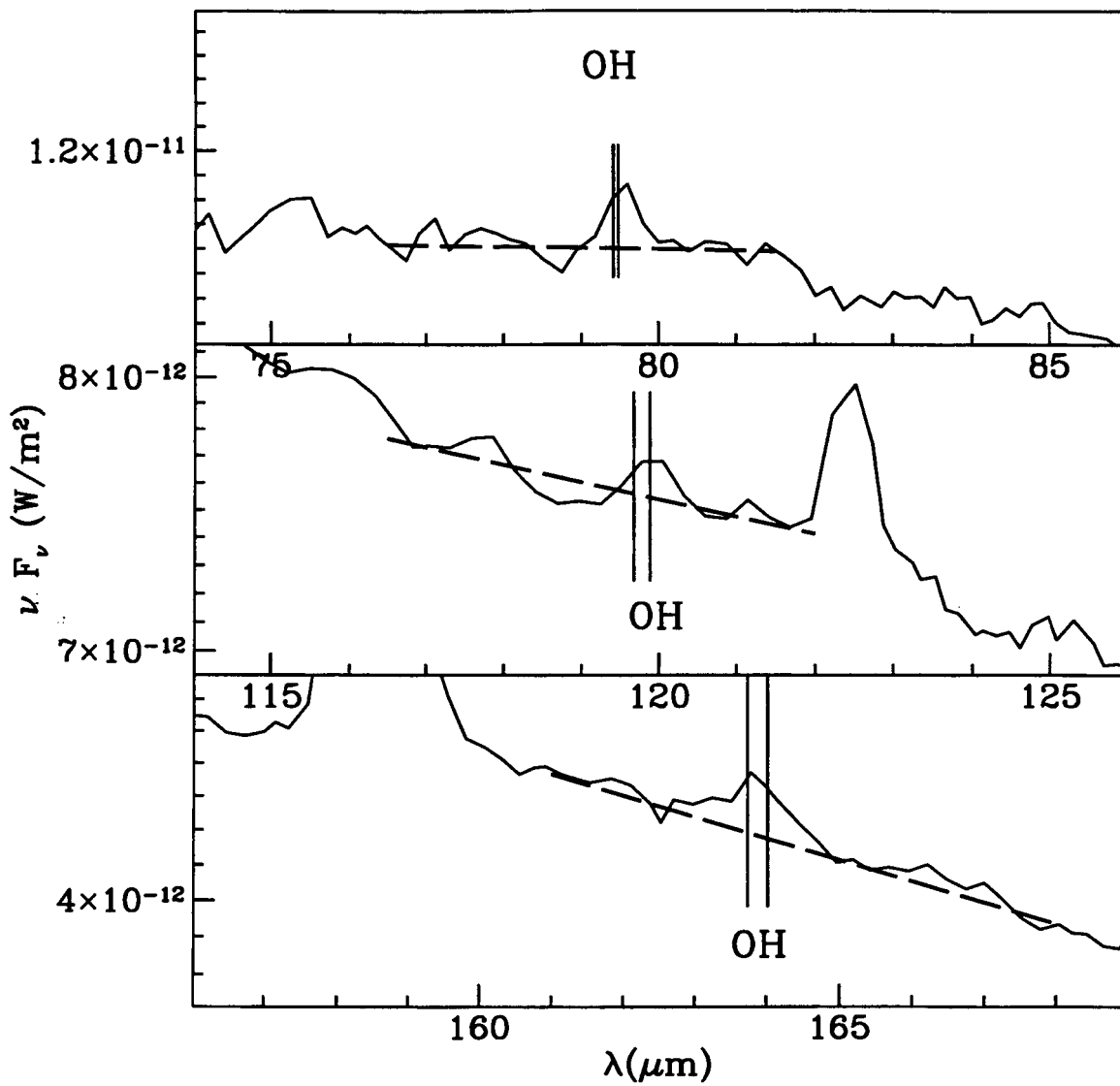


Fig. 6.— The observed emission lines of the OH molecule: from top to bottom: the 79 μ m, the 119 μ m and the 163 μ m lines.

Table 1. Measured line fluxes from the LWS and SWS grating spectra, with 1σ uncertainties.

Line	λ (μm)	Flux ($10^{-13} \text{ erg s}^{-1} \text{ cm}^{-2}$)	Aperture ($''^2$)	reference
[Si IX] $^3P_2 \rightarrow ^3P_1$	2.584	3.0	14×20	1
[Mg VIII] $^2P_{3/2} \rightarrow ^2P_{1/2}$	3.028	$11. \pm 1.1$	14×20	1
[Si IX] $^3P_1 \rightarrow ^3P_0$	3.936	5.0 ± 0.6	14×20	1
[Mg IV] $^2P_{1/2} \rightarrow ^2P_{3/2}$	4.487	7.6 ± 1.5	14×20	1
[Ar VI] $^2P_{3/2} \rightarrow ^2P_{1/2}$	4.529	$15. \pm 3.$	14×20	1
[Fe II] $^4F_{9/2} \rightarrow ^6D_{9/2}$	5.340	5.0	14×20	1
[Mg VII] $^3P_2 \rightarrow ^3P_1$	5.503	13.	14×20	1
[Mg V] $^3P_1 \rightarrow ^3P_2$	5.610	$18. \pm 2.$	14×20	1
[Ar II] $^2P_{1/2} \rightarrow ^2P_{3/2}$	6.985	13.	14×20	1
[Na III] $^2P_{1/2} \rightarrow ^2P_{3/2}$	7.318	5.8	14×20	1
[Ne VI] $^2P_{3/2} \rightarrow ^2P_{1/2}$	7.652	$110. \pm 11.$	14×20	1
[Fe VII] $^3F_4 \rightarrow ^3F_3$	7.815	3.0	14×20	1
[Ar V] $^3P_2 \rightarrow ^3P_1$	7.902	$< 12.$	14×20	1
[Na VI] $^3P_2 \rightarrow ^3P_1$	8.611	$< 16.$	14×20	1
[Ar III] $^3P_1 \rightarrow ^3P_2$	8.991	23.0 ± 3.3	14×20	1
[Fe VII] $^3F_3 \rightarrow ^3F_2$	9.527	4.0	14×20	1
[S IV] $^2P_{3/2} \rightarrow ^2P_{1/2}$	10.510	$58. \pm 6.$	14×20	1
[Ne II] $^2P_{3/2} \rightarrow ^2P_{1/2}$	12.813	70.	14×27	1
[Ar V] $^3P_1 \rightarrow ^3P_0$	13.102	$< 16.$	14×27	1
[Ne V] $^3P_2 \rightarrow ^3P_1$	14.322	$97. \pm 9.7$	14×27	1
[Ne III] $^3P_1 \rightarrow ^3P_2$	15.555	$160. \pm 32.$	14×27	1
[Fe II] $^4F_{7/2} \rightarrow ^4F_{9/2}$	17.936	$< 10.$	14×27	1
[S III] $^3P_2 \rightarrow ^3P_1$	18.713	40.	14×27	1
[Ne V] $^3P_1 \rightarrow ^3P_0$	24.317	$70. \pm 7.$	14×27	1
[O IV] $^2P_{3/2} \rightarrow ^2P_{1/2}$	25.890	$190. \pm 20.$	14×27	1
[Fe II] $^6D_{7/2} \rightarrow ^6D_{9/2}$	25.988	8.	14×27	1
[S III] $^3P_1 \rightarrow ^3P_0$	33.481	55.	20×33	1
[Si II] $^2P_{3/2} \rightarrow ^2P_{1/2}$	34.814	91.	20×33	1
[Ne III] $^3P_0 \rightarrow ^3P_1$	36.013	18.	20×33	1
[O III] $^3P_2 \rightarrow ^3P_1$	51.814	$114. \pm 3.$	80	2
[N III] $^2P_{3/2} \rightarrow ^2P_{1/2}$	57.317	51.4 ± 2.5	80	2
[O I] $^3P_1 \rightarrow ^3P_2$	63.184	$156. \pm 1.$	80	2
[O III] $^3P_1 \rightarrow ^3P_0$	88.356	$111. \pm 1.$	80	2
[N II] $^3P_2 \rightarrow ^3P_1$	121.897	30.5 ± 1.1	80	2
[O I] $^3P_0 \rightarrow ^3P_1$	145.525	11.9 ± 0.4	80	2
[C II] $^2P_{3/2} \rightarrow ^2P_{1/2}$	157.741	$216. \pm 1.$	80	2
OH $^2\Pi_{1/2}5/2-^2\Pi_{3/2}3/2$	34.60/34.63	$< 3.$	20×33	2
OH $^2\Pi_{1/2}1/2-^2\Pi_{1/2}3/2$	79.11/79.18	14.4 ± 1.5	80	2
OH $^2\Pi_{3/2}5/2-^2\Pi_{3/2}3/2$	119.23/119.44	11.9 ± 1.2	80	2
OH $^2\Pi_{1/2}3/2-^2\Pi_{1/2}1/2$	163.12/163.40	7.42 ± 0.65	80	2

Note. — (1): from Lutz et al. (2000) and, where errors are available, Alexander et al. (2000);
(2): this work

Table 2. Comparison of observed line fluxes with AGN model predictions

Line id. λ (μm)	Observed/D ¹ /D ²	Flux (10^{-13} erg s ⁻¹ cm ⁻²)			
		AGN A model ³		AGN B model ⁴	
		Component A	Component B	Component A	Component B
O VI λ .1032+.1037	37.4/4334./402.	91.8+69.5	3.0+2.6	14.5+11.1	0.4+0.4
(Ly α) _n λ .1215	101.8/3562./602	1014.	1412.	733.	1327.
N IV] λ .1487	5.1/103./22.9	25.	9.0	23.6	9.7
(CIV) _n λ .1549	39.7/790./177.	618.	156.	351.	161.
HeII λ .1640	21.4/426./95.5	139.	122.	169.	119.
[Ne V] λ .3426	15.7/95./38.7	103.	34.	58.5	11.6
[Ne III] λ .3869+.3968	19.2/97./43.2	10.4+3.1	53.+16.	17.3+5.2	79.8+24.
HeII λ .4686	6.1/27.6/13.	19.2	17.5	23.9	17.2
[O III] λ .4959+.5007	256./964./496	113.+39.	424.+147	91.5+31.6	486.+168.
[Si VI] λ 1.96	8.0/9.2/8.6	9.3	4.0	9.0	5.0
[Si VII] λ 2.48	8.3	5.1	0.4	6.8	0.8
[Si IX] λ 2.584	3.0	0.7	...	1.0	...
[Mg VIII] λ 3.028	11.	3.0	...	4.6	...
[Si IX] λ 3.936	5.4	1.2	...	1.8	...
[Mg IV] λ 4.487	7.6	4.5	11.1	6.7	10.
[Ar VI] λ 4.529	15.	16.2	14.5	18.7	12.7
[Mg VII] λ 5.503	13.	8.2	0.5	8.8	0.3
[Mg V] λ 5.610	18.	13.4	12.	9.3	6.1
[Ar II] λ 6.985	13.	0.1	1.3
[Na III] λ 7.318	5.8	...	0.55	0.1	0.9
[Ne VI] λ 7.652	110.	111.	17.5	65.8	5.3
[Fe VII] λ 7.815	3.0	3.8	3.7	3.2	2.1
[Ar V] λ 7.902	< 12.	1.8	3.5	3.2	4.0
[Na VI] λ 8.611	< 16.	1.2	0.3	0.8	0.1
[Ar III] + [Mg VII] λ 8.991	25.	0.9+10.	11.1+0.6	1.2+11.0	8.9+0.4
[Fe VII] λ 9.527	4.0	15.6	15.8	13.3	8.9
[S IV] λ 10.510	58.	25.6	86.	29.1	145.
[Ne II] λ 12.813	70.	...	7.3	...	0.9
[Ar V] λ 13.102	< 16.	2.0	5.1	3.3	6.1
[Ne V] λ 14.322	97.	132.	98.	102.	45.9
[Ne III] λ 15.555	160.	3.4	47.	7.1	67.9
[S III] λ 18.713	40.	4.5	40.	2.7	28.3
[Ne V] λ 24.317	70.	58.	77.	42.3	35.4
[O IV] λ 25.890	190.	38.5	104.	58.2	105.
[S III] λ 33.481	55.	1.0	22.	0.6	15.7
[Si II] λ 34.814	91.	...	1.5	...	0.8
[Ne III] λ 36.013	18.	0.2	4.0	0.5	5.8
[O III] λ 51.814	110.	1.8	42.	1.7	48.
[N III] λ 57.317	51.	0.7	14.5	0.6	13.
[O I] λ 63.184	156.
[O III] λ 88.356	110.	0.2	10.2	0.2	11.6
[N II] λ 121.897	30.	...	0.2
[O I] λ 145.525	12.
[C II] λ 157.741	220.	...	0.3

¹Dereddened line flux, assuming $E_{B-V} = 0.4$

²Dereddened line flux, assuming $E_{B-V} = 0.2$

³AGN A parameters: component A: Log U=-1., Log n=4, internal radius $\simeq 19$ pc, external radius $\simeq 80$ pc, ionizing spectrum from Alexander et al. (2000); component B: Log U=-2., Log n=3.3, internal radius $\simeq 140$ pc, external radius $\simeq 190$ pc, ionizing spectrum from Alexander et al. (2000).

⁴AGN B parameters: same as AGN A models, but with the ionizing spectrum from Pier et al. (1994)

Table 3. Comparison of observed line fluxes with AGN and SBN model predictions

Line id. λ (μm)	Observed/D ¹ /D ²	Flux (10^{-13} erg s ⁻¹ cm ⁻²)		SBN F ⁶	SBN E ⁷
		AGN C model ³	Component A		
O VI λ .1032+.1037	37.4/4334./402.	65.3+34.8	6.6+3.5	...	0.25+0.15
(Ly α) _n λ .1215	101.8/3562./602	701.	1180.
N IV] λ .1487	5.1/103./22.9	21.4	18.1
(CIV) _n λ .1549	39.7/790./177.	384.	718.
HeII λ .1640	21.4/426./95.5	147.	308.	75.	108.
[Ne V] λ .3426	15.7/95./38.7	115.	152.	...	10.9
[Ne III] λ .3869+.3968	19.2/97./43.2	2.0+0.6	14.8+4.4	42.+12.	43.+13.
HeII λ .4686	6.1/27.6/13.	20.	43.4	11.3	16.
[O III] λ .4959+.5007	256./964./496	13.4+4.6	112.+39	29.+83.	156+452
[Si VI] λ 1.96	8.0/9.2/8.6	10.3	8.7
[Si VII] λ 2.48	8.3	6.2	0.9
[Si IX] λ 2.584	3.0	0.4
[Mg VIII] λ 3.028	11.	3.6
[Si IX] λ 3.936	5.4	0.7
[Mg IV] λ 4.487	7.6	3.0	13.3	...	4.9
[Ar VI] λ 4.529	15.	18.9	52.6
[Mg VII] λ 5.503	13.	11.2	1.7
[Mg V] λ 5.610	18.	13.3	34.5	...	5.3
[Ar II] λ 6.985	13.	6.0	2.0
[Na III] λ 7.318	5.8	0.8	0.5
[Ne VI] λ 7.652	110.	171.	102.	...	5.6
[Fe VII] λ 7.815	3.0	3.4	9.2
[Ar V] λ 7.902	< 12.	1.7	8.0	...	1.2
[Na VI] λ 8.611	< 16.	1.4	1.4	...	0.25
[Ar III] + [Mg VII] λ 8.991	25.	... +13.6	0.8+2.2	20.+ ...	7.3+ ...
[Fe VII] λ 9.527	4.0	13.7	38.7
[S IV] λ 10.510	58.	13.5	104	1.3	41.6
[Ne II] λ 12.813	70.	7.1	2.5
[Ar V] λ 13.102	< 16.	1.8	11.8	...	2.2
[Ne V] λ 14.322	97.	133.	355.	...	43.8
[Ne III] λ 15.555	160.	0.5	5.6	59.	38.
[S III] λ 18.713	40.	0.5	5.8	21.3	22.6
[Ne V] λ 24.317	70.	59.4	280	...	48.
[O IV] λ 25.890	190.	22.	217.	3.3	207.
[S III] λ 33.481	55.	0.1	3.3	32.7	34.8
[Si II] λ 34.814	91.	...	0.1	155.	60.
[Ne III] λ 36.013	18.	...	0.5	5.2	3.4
[O III] λ 51.814	110.	0.2	5.9	16.7	59.
[N III] λ 57.317	51.	0.1	2.7	5.9	21.2
[O I] λ 63.184	156.	25.1	8.
[O III] λ 88.356	110.	...	1.5	26.6	104.
[N II] λ 121.897	30.	7.0	2.5
[O I] λ 145.525	12.	2.4	0.8
[C II] λ 157.741	220.	67.5	38.5

¹Dereddened line flux, assuming $E_{B-V} = 0.4$

²Dereddened line flux, assuming $E_{B-V} = 0.2$

³AGN C parameters: same as AGN A models, but with the ionizing spectrum that includes a big blue bump (see text)

⁴SBN F parameters: Log U=-3.5, Log n=1.3, ionizing spectrum from Starburst99 continuous model with Z=.008 and duration of 50 Myr. The integration was stopped at a temperature of 50K.

⁵SBN E parameters: Log U=-2.5, Log n=0.3, ionizing spectrum from Starburst99 continuous model with Z=.008 and duration of 50 Myr. The integration was stopped at a temperature of 50K.

Table 4. Comparison of observed line fluxes with Ring Starburst model predictions

Line id.λ (μm)	Observed	Flux (10^{-13} erg s $^{-1}$ cm $^{-2}$)					
		SBR A ¹	SBR B ²	SBR C ³	SBR D ⁴	SBR E ⁵	SBR F ⁶
[Ne II] λ 12.813	70.	1.2	1.5	1.0	1.2	0.3	1.1
[Ar V] λ 13.102	< 16.	0.3	...
[Ne V] λ 14.322	97.	0.6	...
[Ne III] λ 15.555	160.	11.2	11.4	8.7	8.8	5.7	9.0
[S III] λ 18.713	40.	3.9	3.7	3.2	3.0	3.4	3.2
[Ne V] λ 24.317	70.	7.3	...
[O IV] λ 25.890	190.	0.5	0.4	31.	0.5
[S III] λ 33.481	55.	13.3	12.9	11.1	11.	12.	11.3
[Si II] λ 34.814	91.	65.8	75.2	52.4	58.4	20.9	53.8
[Ne III] λ 36.013	18.	2.2	2.3	1.8	1.8	1.1	1.8
[O III] λ 51.814	110.	4.2	3.7	16.5	14.7	54.8	15.3
[N III] λ 57.317	51.	1.5	1.4	5.9	5.6	19.5	5.4
[O I] λ 63.184	156.	32.	36.6	21.7	24.3	7.3	22.
[O III] λ 88.356	110.	7.0	6.5	26.6	25.9	95.8	24.7
[N II] λ 121.897	30.	8.2	8.0	6.1	6.2	2.4	6.7
[O I] λ 145.525	12.	3.1	3.6	2.1	2.3	0.7	2.2
[C II] λ 157.741	220.	76.3	142.	60.	107.	35.	62.3

¹SBR A parameters: Log U=-3.5, Log n=1.3, ionizing spectrum from Starburst99 instantaneous model with Z=.008 and duration of 5 Myr. The integration was stopped at a temperature of 50K.

²SBR B parameters: Log U=-3.5, Log n=0.3, ionizing spectrum from Starburst99 instantaneous model with Z=.008 and duration of 5 Myr. The integration was stopped at a temperature of 50K.

³SBR C parameters: Log U=-3.5, Log n=1.3, ionizing spectrum from Starburst99 continuous model with Z=.008 and duration of 5 Myr. The integration was stopped at a temperature of 50K.

⁴SBR D parameters: Log U=-3.5, Log n=0.3, ionizing spectrum from Starburst99 continuous model with Z=.008 and duration of 5 Myr. The integration was stopped at a temperature of 50K.

⁵SBR E parameters: Log U=-2.5, Log n=0.3, ionizing spectrum from Starburst99 continuous model with Z=.008 and duration of 50 Myr. The integration was stopped at a temperature of 50K.

⁶SBR F parameters: Log U=-3.5, Log n=1.3, ionizing spectrum from Starburst99 continuous model with Z=.008 and duration of 50 Myr. The integration was stopped at a temperature of 50K.

Table 5. Comparison of observed line fluxes with composite model predictions

Line id. λ (μm)	Flux (10^{-13} erg s^{-1} cm^{-2})			
	Observed/ D^1/D^2	CM1 ³	CM2 ⁴	CM3 ⁵
O VI λ .1032+.1037	37.4/4334./402.	170.	26.4	110.2
(Ly α) _n λ .1215	101.8/3562./602	2426.	2060.	1881.
N IV] λ .1487	5.1/103./22.9	34.	33.3	39.5
(CIV) _n λ .1549	39.7/790./177.	774.	512.	1102.
HeII λ .1640	21.4/426./95.5	336.	363.	530.
[Ne V] λ .3426	15.7/95./38.7	137.	70.1	267.
[Ne III] λ .3869+.3968	19.2/97./43.2	137.4	180.3	75.8
HeII λ .4686	6.1/27.6/13.	48.	52.4	74.7
[O III] λ .4959+.5007	256./964./496	835	889.	281.
[Si VI] λ 1.96	8.0/9.2/8.6	13.3	14.	19.
[Si VII] λ 2.48	8.3	5.5	7.6	7.1
[Si IX] λ 2.584	3.0	0.7	1.0	0.4
[Mg VIII] λ 3.028	11.	3.0	4.6	3.6
[Si IX] λ 3.936	5.4	1.2	1.8	0.7
[Mg IV] λ 4.487	7.6	15.6	16.7	16.3
[Ar VI] λ 4.529	15.	30.7	31.4	71.5
[Mg VII] λ 5.503	13.	8.7	9.1	12.9
[Mg V] λ 5.610	18.	25.4	15.4	47.8
[Ar II] λ 6.985	13.	7.4	6.0	6.0
[Na III] λ 7.318	5.8	1.4	1.8	0.8
[Ne VI] λ 7.652	110.	128.5	71.1	273.
[Fe VII] λ 7.815	3.0	7.5	5.3	12.6
[Ar V] λ 7.902	< 12.	5.3	7.2	9.7
[Na VI] λ 8.611	< 16.	1.5	0.9	2.8
[Ar III] + [Mg VII] λ 8.991	25.	42.6	41.5	36.6
[Fe VII] λ 9.527	4.0	31.4	22.2	52.4
[S IV] λ 10.510	58.	113.	175.3	118.8
[Ne II] λ 12.813	70.	14.7	8.3	7.4
[Ar V] λ 13.102	< 16.	7.4	9.7	13.9
[Ne V] λ 14.322	97.	230.6	148.6	488.6
[Ne III] λ 15.555	160.	115.1	140.	70.8
[S III] λ 18.713	40.	69.2	55.7	30.7
[Ne V] λ 24.317	70.	142.3	85.	346.7
[O IV] λ 25.890	190.	177.	197.5	273.3
[S III] λ 33.481	55.	67.7	61.	48.1
[Si II] λ 34.814	91.	177.4	177.	176.
[Ne III] λ 36.013	18.	10.5	12.6	6.8
[O III] λ 51.814	110.	115.5	121.2	77.6
[N III] λ 57.317	51.	40.6	39.	28.2
[O I] λ 63.184	156.	32.4	32.4	32.4
[O III] λ 88.356	110.	132.8	134.	123.9
[N II] λ 121.897	30.	9.6	9.4	9.4
[O I] λ 145.525	12.	3.1	3.1	3.1
[C II] λ 157.741	220.	103.	102.5	102.5

¹Dereddened line flux, assuming $E_{B-V} = 0.4$

²Dereddened line flux, assuming $E_{B-V} = 0.2$

³CM1 = AGN A + SBN F + SBR E

⁴CM2 = AGN B + SBN F + SBR E

⁵CM3 = AGN C + SBN F + SBR E

Table 6. Comparison of observed line fluxes with OH montecarlo model predictions

Line id. λ	Flux (10^{-12} <i>erg s⁻¹ cm⁻²</i>)		Notes
	Observed	Modeled	
34 μ m	< .5	-0.5	(absorption)
48 μ m	...	0.12	
53 μ m	< 1.2	-0.4	(absorption)
65 μ m	< 1.2	0.2	
79 μ m	1.44	1.10	
84 μ m	< 1.2	0.5	
96 μ m	...	0.3	
98 μ m	< 1.2	0.4	
115 μ m004	
119 μ m	1.19	1.31	
163 μ m	0.74	0.60	